![Cambridge University Press logo]

Metamorphic P-T evolution and tectonic implications of UHT metamorphism from the Shillong Meghalaya Gneissic Complex, India: evidence from phase equilibria modelling, monazite U-Pb-Th geochronology, K-Ar dating and geochemistry

Bikash Mahanta[1], Divya Prakash[1] ![ORCID], Saurabh Singh[1], C.K. Singh[1], Manish Kumar[1], Rajeev Pandey[1] and Suparna Tewari[2] ![ORCID]

[1]Centre of Advanced Study in Geology, Banaras Hindu University, Varanasi – 221005; India and [2]Central University of Punjab, Bathinda-151001, India

Abstract

The study area Sonapahar is an integral part of Shillong Meghalaya Gneissic Complex (SMGC), which is located in the Northeastern part of India. This complex mainly comprises metamorphic formations spanning from Upper Amphibolite to Ultra-high temperature granulite, interspersed with various igneous intrusions. In this study, particular attention is directed towards unravelling the metamorphic history of Mg-Al granulite. For the very first time, we establish the pressure–temperature (P-T) trajectory of the Mg-Al granulite from Sonapahar, SMGC. Employing conventional thermobarometry along with winTWQ analysis, the inferred metamorphic conditions for this granulite reveal temperatures exceeding 900°C and pressures of approximately >8 kbar. These conditions firmly indicate the presence of ultra-high-temperature metamorphism. By utilizing the Perple_X software in the MnO-Na$_2$O-CaO-K$_2$O-FeO-MgO-Al$_2$O$_3$-SiO$_2$-H$_2$O-TiO$_2$-Fe$_2$O$_3$ compositional system, we construct a P-T pseudosection. This gives a clockwise P-T path, signifying an episode of cooling (+ minor decompression). Such a pattern also suggests rapid cooling of the tectonically-thickened crust. Concurrently, a geochemical exploration of trace and rare earth elements in the rocks offers further insights. These investigations give an idea about the protolith, having a clay-to-sandstone in nature. Additionally, chemical data from monazite within the studied rock provide a weighted mean age of 682 Ma for the peak metamorphic stage. This age aligns with the global Pan-African orogenic events. The biotite K-Ar isotopic geochronology from the symplectite position provides decompression history or cooling age of 442 Ma. This age corresponds to a period after the last peak metamorphic phase that occurred during the Pan-African thermal event.

1. Introduction

Granulites serve as a window into the deep crust by being exposed in high-grade regional metamorphic terranes. They thus play a critical role in constraining theories of crustal processes and evolution. Understanding granulites not only enables us to set limits on the nature and makeup of the lower crust of the existing continents, but it also provides insight into the dynamic tectonic and chemical processes that result in the accumulation and eventual stabilization of the changing aspects of the current crust, which in turn supports continental growth.

The principal objective of this research is to study the complex tectono-metamorphic evolution of the Mg-Al granulite, encompassing petrology, mineral chemistry, geochronology and geochemical characteristics. Using mineral chemistry data and employing various thermobarometric techniques and software, such as winTWQ, we aim to deduce the progressive history of pressure–temperature (P-T) conditions associated with distinct metamorphic stages. Furthermore, the integration of X-ray fluorescence (XRF) data derived from whole rock samples, interpreted through software platforms like Perple_X, is utilized to narrow down the trajectories of equilibrium phases during both peak and post-peak metamorphic phases. An additional aspect of this study involves shedding light on the broader tectonic implications and the inherent nature of the protolith. This is achieved through the examination of rare earth element (REE) and trace element data, which provide valuable insights into the geological processes that have influenced the formation and transformation of the pelitic granulite. Notably, despite the existing records of monazite geochronology (Mahanta *et al.* 2024,

Chatterjee et al. 2007, 2011) from other rock types in the Sonapahar region revealing a diverse spectrum of metamorphic and magmatic phenomena, the pelitic granulites have not received adequate attention in terms of geochronological investigations.

The studied Mg-Al granulites have been previously studied by Lal et al. (1978). Revisiting and re-evaluating the P–T conditions of these rocks is crucial to understanding the metamorphic history and tectonic evolution of the region. By employing modern analytical techniques and advanced software programs such as PerpleX and WinTWQ, this study aims to provide a more accurate and comprehensive interpretation of the metamorphic conditions experienced by these granulites. Our study is the first to provide integrated results from phase equilibria modelling, geochemistry and monazite U-Pb geochronology, where we identify continental island arc protolith sources subjected to the common Neoproterozoic high to ultra-high temperature (UHT) metamorphism from the central part of this block, although previous studies have not reported UHT metamorphism from Shillong Meghalaya Gneissic Complex (SMGC) (viz., Lal et al. 1978, Chatterjee et al. 2007). Our findings offer ideas on the P-T path (prograde, peak and retrograde metamorphism) as well as the peak metamorphism timing. Our research provides additional proof of metamorphism from high to ultra-high temperatures, which is linked to the collisional assembly of the Gondwana supercontinent in the Late Neoproterozoic period.

2. Geological settings

The SMGC, a relatively less studied metamorphic terrain, is located in the northeastern region of India. This complex serves as the foundational base for several significant granulitic terrains, which need detailed scientific study. Spanning an east-west trending expanse of 40000 km^2, the SMGC holds essential geological importance. The Dhansiri (Jamuna) fault runs north-south, separating it from the Indian shield (Evans 1964 and Nandy 1980).

Additionally, it is suggested by Evans (1964) and Desikachar (1974), as well as Crawford (1974), that the Chotanagpur Gneissic Complex (CGC) or the Eastern Ghats Mobile Belt (EGMB) could potentially be extensions of the SMGC in its western direction. The SMGC is composed of a complex group of rocks that includes (a) Archean to Paleoproterozoic Gneissic rocks, as reported by Bidyananda and Deomurari (2007), Chatterjee et al. (2007, 2011), and Kumar et al. (2017a); (b) Shillong Group metasediments from the Paleoproterozoic to Mesoproterozoic periods, as proposed by Mitra (1998) and Bidyananda and Deomurari (2007) and (c) Proterozoic to Paleozoic granitoids, characterized by igneous intrusions, as reported by Ghosh et al. (1991, 1994, 2005). According to Sengupta and Agarwal (1998) and Nandy (2001), the SMGC is geologically surrounded by important tectonic features, such as the Rajmahal-Garo tectonic graben on its western edge, a belt of Schuppen to its eastern side, the Brahmaputra lineament to its north and the Dauki tear fault marking its southern boundary.

The Archean to Paleoproterozoic Gneissic Complex, commonly referred to as the Basement Gneissic Complex of the SMGC, comprises a diverse range of rock types. These include Precambrian gneisses, amphibolites, granulites (rich in garnet, cordierite and sillimanite), basic granulites, calc-silicate gneisses and a collection of granitoids. These lithologies collectively form a basement layer for the geological evolution of the region (Chatterjee et al. 2007). Overlying the Basement Gneissic Complex are the metasediments belonging to the Shillong Group. Notably, between 1862 ± 63 Ma and 497 ± 9 Ma SMGC witnessed multiple episodes of granitic

emplacement, as suggested by Bidyananda and Deomurari (2007), Yin et al. (2010), and Kumar et al. (2017a, b). These chronological events have contributed significantly to shaping the geological structure of the SMGC (Fig. 1a).

A notable geological feature that distinguishes the study area (Sonapahar) is the dominance of felsic and mafic rock granulites (Fig. 1b). According to Lal et al. (1978) and Chatterjee et al. (2007, 2011), this geological configuration is recognized as a key part of the Central SMGC. The primary minerals found in the felsic rock are spinel, cordierite and garnet, which are encased in a matrix of k-feldspar, plagioclase and quartz. The mafic granulite, in contrast, is abundant in minerals like orthopyroxene, clinopyroxene, biotite, sillimanite, spinel, rutile and ilmenite. The granulite facies rocks from the Sonapahar region also contain the relics of greenschist facies metapelites from the Shillong Group, as outlined by Nandy (2001). According to Lal et al. (1978), the peak metamorphic conditions experienced by the Sonapahar area are at 750°C and 5 kbar from the study of sapphirine-bearing metapelites. Neogi and Pal (2021) investigated the geological history of the Sonapahar rocks, revealing a complex pattern of tectonic disturbances that the region has experienced. They established the occurrence of three separate stages of tectonic activity by analyzing the orientations of tectonic fabrics (both planar and linear) present within the rock formations. This finding gives an idea about the dynamic geological evolution of the Sonapahar area.

3. Analytical methods

3.a. Petrography

Petrographic and thin section studies were carried out using the Leica (DM 2500P) microscope at the Metamorphic Petrology Laboratory, Department of Geology at Banaras Hindu University, for comprehensive petrographic analysis. Subsequent microphotographs were also taken using the same range of microscope.

3.b. Mineral chemistry

Electron microprobe analyses and backscattered electron imaging were carried out using the CAMECA SXFive electron probe micro analyzer (EPMA) instrument in conjunction with the advanced SXFive software in the DST-SERB National Facility, Department of Geology (Center of Advanced Study), Institute of Science, Banaras Hindu University. The LEICA-EM ACE200 apparatus was used to apply a 20 nm thick carbon coating, which was administered to prepare the thin sections for their microprobe excursion. An accelerating voltage of 15 kV and a beam current of 10 nA were used with analytical precision. To establish an internal reference, the crystal positions were checked using the natural silicate mineral andradite. The routine silicate quantification process utilizes natural mineral standards, including diopside, peridot, almandine, albite and orthoclase, which are supplied by CAMECA-AMETEK. The SxSAB version 6.1 and SX-Results application from CAMECA were used to carry out regular calibration, collection, quantification and data processing. The precision of the results was below the threshold of 1% for major element oxides and 5% for trace elements.

3.c. Geothermobarometry

P-T conditions were calculated using thermodynamic data by Berman and Aranovich (1996, updated December 2006) and the internally consistent winTWQ program (Rob Berman, 2006,
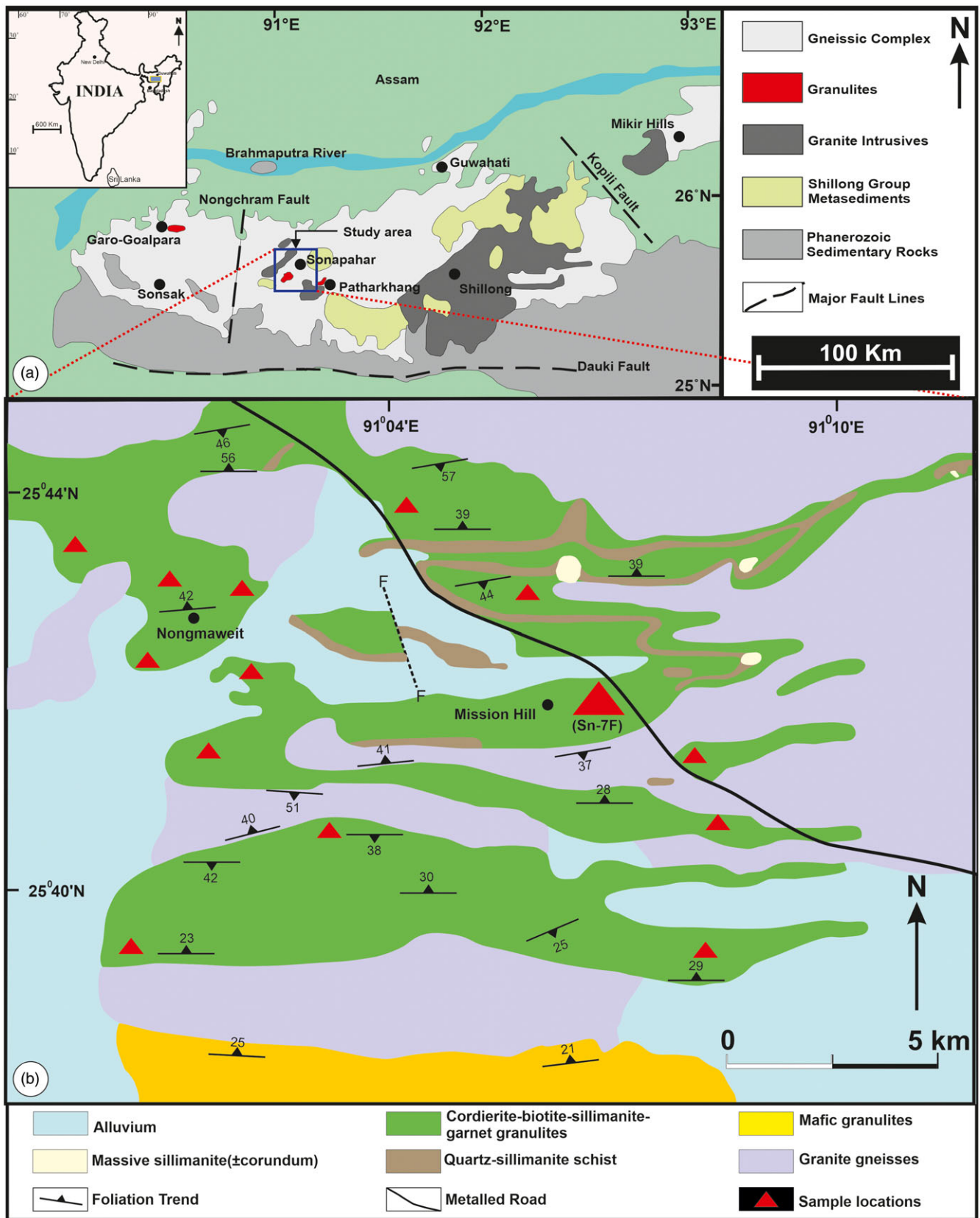
Figure 1. (a) Geological map of Shillong Meghalaya Gneissic Complex (SMGC) (modified after Dwivedi *et al.* 2020), (b) geological map of Sonapahar (Riangdo) area of central SMGC (modified after Lal *et al.* 1978).

version 2.32). In conventional thermobarometry, a range of methodologies have been utilized to decipher the pressure and temperature conditions that rocks have undergone. Temperature calculations were performed using the Fe-Mg exchange between garnet–cordierite and Fe-Mg exchange between garnet–biotite thermometers as described by Bhattacharya et al. (1992) and Thompson (1976). In contrast, garnet–sillimanite–plagioclase–quartz and garnet–cordierite–sillimanite–quartz have been taken into consideration for barometer calculations.

3.d. Whole-rock geochemistry (XRF) and phase equilibria modelling

The complex mineral phase equilibria computations were made possible by the XRF data. The Perple_X program (version 6.9.1) was used to carry out these computations (Connolly, 2005 and Connolly, 2009). The model system, MnNCKFMASHTO (MnO-Na2O–CaO–K2O–FeO–MgO–Al2O3–SiO2–H2O–TiO2–Fe2O3), was used to address the complexities of the system under study. Based on the observed mineral assemblage, an extensive range of solution models has been considered while preparing the P-T pseudosection. These models include Gt(W) for garnet (White *et al.* 2014), Crd(W) for cordierite (White *et al.* 2014), Bi(W) for biotite (White *et al.* 2014), the ternary model "feldspar_B" for feldspar (Benisek *et al.* 2010), Sp(WPC) for spinel (White *et al.* 2002), St(W) for staurolite (White *et al.* 2014), Ilm(DS6) for ilmenite (Holland and Powell, 2011), Mica(W) for mica (White *et al.* 2014) and melt(W) for melt phases (White *et al.* 2014). The thermodynamic dataset, by Holland and Powell in 1998, subsequently revised in 2011, was employed.

The Siemens SRS-3000 WD-XRF instrument was used for the XRF analysis at the Birbal Sahni Institute of Palaeosciences (BSIP) in Lucknow, India. Several standards are used, including BHVO-2, BCR2, BIR-1a, JA2, JGb-1, JGb-2, MBH and others. For the pseudosection modelling, the bulk rock data sample which is near to the average of all the twenty samples (Sn-7F, 1–20) from the XRF analysis was used (Table. 3). However, the quantification of the presence of H_2O was facilitated by the utilization of the loss of ignition (LOI) value. The O2 value was derived by preparing a T-X(Fe^{3+}) diagram and recalculating the XRF bulk rock data using the recalc-for-PerpleX datasheet.

3.e. Whole rock geochemistry (ICPMS)

Twenty representative samples from different parts of outcrop Sn-7F (Sn-7F/1 to Sn-7F/20) were selected for analysis of whole-rock geochemical data (trace elements and REE) at the Birbal Sahni Institute of Palaeosciences, Lucknow, India. Homogenized samples were ground to a size of around 200 mesh in an agate mortar. The powdered samples were completely mixed with hydrogen borate powder in the desired proportion before being formed into pressed pellets using a motorized press (Kameyo Delta TP02). Agilent 7700 ICP-MS technology was used to assess the trace element as well as REE content in the samples. The ASTM D6357-11 method was used to break down the materials. Before ICP-MS elemental analysis, and samples are digested using trace element acids such as hydrofluoric (HF), nitric acid (HNO3) and hydrochloric acid (HCl). In addition to certain internal standards, several standards from the USGS and the Wadia Institute of Himalayan Geology, India (including BCR2, BHVO-2, BIR-1a, SL-1 and MBH) were used for calibration. With a muffle furnace, the LOI was determined.

3.f. K-Ar dating

Biotite grains from the symplectitic textural location of the Mg-Al granulite sample Sn-7F have been studied using an efficient K-Ar isotopic analysis approach, as described by Solé in 2014. The analysis was carried out at the Instituto de Geología, Universidad Nacional Autónoma de México, Mexico.

3.g. Monazite chemical dating

The monazite chemical dating was accomplished by examining the prominent subhedral to anhedral grains of monazite using the EPMA CAMECA SX-Five instrument facilities at the Department of Geology (Centre of Advance Study), Institute of Science, Banaras Hindu University. We used the most recent analytical method for U-Th-Pb monazite dating, by Pandey et al. (2019). The polished thin section of representative sample Sn-7F was coated with a fine layer (20 nm) of carbon using the LEICA-EM ACE 200 carbon coating device. A LaB6 generator in an electron cannon is used to produce an electron beam at an operating voltage of 15 kV at 200 nA.

4. Results

4.a. Petrography

Representative samples of Mg-Al granulite were collected from exposures in road cuttings or stone quarries around Sonapahar village (refer to Fig 2). The distinguishing characteristics of the Mg-Al granulite in the study area are marked by its fine-grained texture (Fig. 2c). The rock is primarily composed of garnet (5%–10%), cordierite (20%–30%), quartz (10%–15%), plagioclase (8%–11%) and K-feldspar (3%–6%), with minor ilmenite (< 1%), spinel (2%–4%), opaques (1%–2%), biotite (5%–10%) and fine-grained sillimanite (1%). The presence of rutile is very scarce, mainly found in two or three places in the thin section. Garnet occurs as porphyroblast structures that contain inclusions of biotite, sillimanite and quartz, and it does not exhibit any distinct compositional zoning (Fig. 3, a–b). The spinel present in the rock displays well-defined grain boundaries that it shares with quartz (Fig. 3, c–d). Cordierite on the other hand occurs as medium- to coarse-grained poikiloblasts becoming the most abundant ground mass mostly associated with feldspar. The feldspar grains tend to be of medium to large size (1–4 mm) and commonly serve as hosts for biotite and sillimanite inclusions (Fig. 3, b–c). Sillimanite is densely intergrown with biotite, resembling needle-like or fibrolitic structures. The majority of the time, these sillimanite needles are discovered inside cordierite porphyroblasts and associated with biotite flakes. Garnet porphyroblasts, as seen in the matrix, and one in symplectite textures are frequently found next to cordierite or with sillimanite inclusions. The presence of a symplectite structure consisting of biotite, sillimanite and quartz with decomposed garnet (Fig. 3, e–f).

4.b. Mineral Chemistry

4.b.1. Garnet

The evaluated garnet samples exhibit X_{Mg} value, ranging from 0.14 to 0.16, signifying a solid solution between almandine and pyrope end-members. The Al content within the garnet samples measures approximately 1.9 a.p.f.u. (Table. 1). To represent these garnet compositions, a triangular diagram was constructed, depicting the relationship between end members (Ca+Mn):Mg: Fe (Fig. 4a).

Figure 2. (a) Field photograph showing the exposure of MG-Al granulite in a rock quarry, (b) photograph showing contact between Mg-Al granulite and massive sillimanite in a sillimanite mine, (c) photograph showing the Mg-Al granulite, (d) close view of Mg-Al granulite showing quartz and cordierite association.

4.b.2. Cordierite

The X_{Mg} values attributed to cordierite range from 0.69 to 0.72, thus indicating a substantial magnesium content. Certain data points in cordierite show slightly lowered totals (97%), a phenomenon that can be attributed to the possible presence of H_2O and/or CO_2, as reported by Hörmann *et al.* (1980) and Lonker (1981). Zoning variations are not prominent in these samples. Negligible quantities of Na_2O are detected, with values reaching up to 0.18 wt% and 0.37 wt%, respectively. Conversely, K_2O remains below the limit of detection (Table. 1).

4.b.3. Feldspar

The compositions of feldspar were shown on a triangular diagram involving the end-members An, Or and Ab (Fig. 4b). Examination of alkali feldspar plots confirms the presence of orthoclase. The An-Ab solid solution indicates that the plagioclase belongs to the albite-oligoclase composition range. The X_K [=K/(Ca + Na + K)] values range from 0.863 to 0.890, and the highest anorthite content extends up to 0.22. Iron, calculated as FeO, is mostly below detectable levels, barring one exception. The same trend holds for TiO_2, MnO and MgO. Cr_2O_3 content spans from 0.2 to 0.3 wt% (Table. 2).

4.b.4. Biotite

Variability in X_{Mg} values is observed across intermediate biotite samples, ranging from 0.37 to 0.54, whereas for Mg-rich biotite (i.e. phlogopite), it is around 0.80. The Ti content within biotite samples shows variations from 0.22 to 1.24. Al content within biotite falls within the range of 2.84 to 3.32 (Table. 2). The composition of biotite (inclusions and symplectites) is shown using X_{Mg} vs Al^{total} (Fig. 4c). Biotite, which is associated with symplectite

texture, is mostly Mg-rich in nature, whereas intermediate biotite is found to occur in almost all textural positions.

4.b.5. Spinel

The spinel present in the analysed sample predominantly constitutes a solid solution between spinel and hercynite, with X_{Mg} values ranging from 0.22 to 0.27 (Table. 2). The spinel composition concerning Zn, Fe and Mg content as end members is shown in Fig. 4d.

4.b.6. Sillimanite

The majority of the observed sillimanite grains were present as inclusions. They show significant levels of FeO, occasionally reaching up to 0.4 wt%. Except for one, Cr_2O_3 content ranges between 0.3 and 0.4 wt%. MnO and MgO remain undetectable, while the average TiO_2 content is around 0.2 wt%.

4.c. P-T pseudosection modelling

The application of XRF analysis to average bulk rock data has played an essential role in determining invaluable insights into the mineralogical composition of representative rock samples. The sample Sn-7F has shown a diverse range of minerals, from garnet, cordierite and K-feldspar to plagioclase, biotite, sillimanite, spinel and quartz. The analytical yielded weight percentages corresponding to a range of oxides, including Na_2O, MgO, Al_2O_3, SiO_2, K_2O, CaO, TiO_2, MnO, FeO^t and LOI (Table. 3). We have considered the sample (Sn-7F/7) containing bulk rock composition near the mean of 20 samples from Sn-7F for constructing the pseudosection. The bulk rock data used for the pseudosection modelling in molar amount are (Na_2O – 1.15, MgO – 8.40, Al_2O_3 – 10.44, SiO_2 – 66.00, K_2O – 2.34, CaO – 0.74, TiO_2 – 0.54, MnO – 0.09, FeO^t – 6.50,
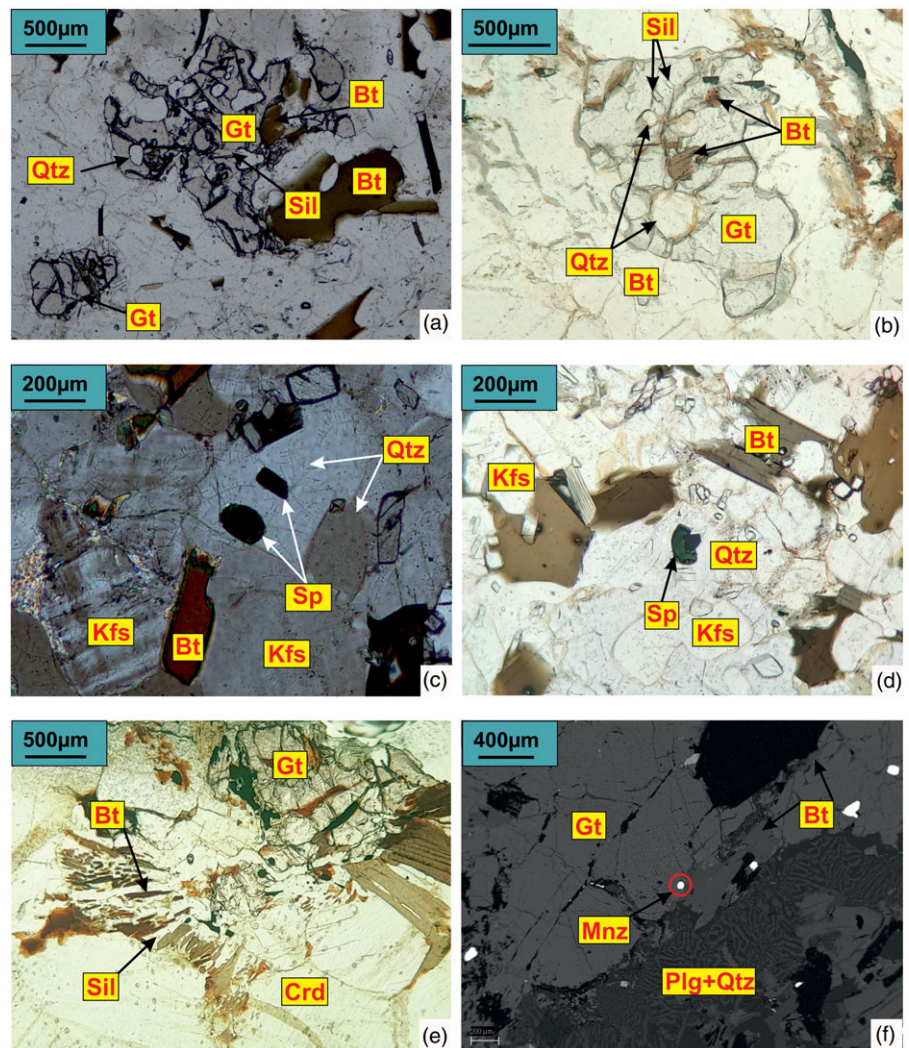
Figure 3. Photomicrographs of the representative sample in plane polarised light showing the evidence of prograde (a-b), peak (c-d) and retrograde (e-f) stages of ultra-high temperature metamorphism.

H_2O – 3.15 and O_2 – 0.65). The O_2 value has been estimated using a T-X(Fe^{3+}) plot (Fig. S1; in the online Supplementary Material available at http://journals.cambridge.org/geo). The pressure (P) and temperature (T) considered in these computations spanned 5–11 kbar and 700–1100 °C, respectively. An important part of these calculations was the incorporation of titanium (Ti), given its profound influence on the stability of biotite. The result of these calculations emerged in the form of pseudosection and provided a thorough understanding of the stability of mineral assemblages under various pressure-temperature (P-T) conditions. The stability fields were represented using various colours to indicate different variance levels (Fig. 5a).

The pseudosection was further contoured with model proportions of garnet, biotite, spinel and cordierite. This shows the dynamic shifts in the proportions of these minerals with respect to temperature. The proportions of garnet and spinel exhibited a direct correlation with temperature. Cordierite growth in modal abundances with the decrease in pressure, whereas biotite growth proportional to decrease in temperature describes the formation of symplectite in the retrograde phase (Fig. 5b).

The delineation of the peak mineral assemblage is based on the petrographical evidence with a temperature estimate of 870°C (HT) at 7.8 kbar, as represented in Fig. 6a (blue dashed line). The

peak metamorphic assemblage is characterized by the presence of spinel, biotite, garnet, sillimanite, feldspar, and quartz. Whereas the retrogradational trajectory of the granulites is based upon the implementation of compositional isopleths of X_{Mg} garnet, X_{Mg} biotite, X_{Mg} cordierite, and X_{Mg} spinel (Fig. 6a). According to the models and petrological evidence, X_{Mg} in garnet and biotite matches for the retrograde P-T estimates mostly demonstrate cooling (+ minor decompression) of the studied sample from 850° C, maybe somewhere between 6 and 8 kbar. Prograde sillimanite in garnet may have grown at these pressures at slightly lower T.

The stability of biotite across the compositional range was maintained, yet its X_{Mg} values exhibited variation in the matrix due to re-equilibration at lower temperatures. This pseudosection further gives the retrograde mineral assemblage at around 700°C at 5.50 kbar.

The constructed pseudosection reveals a minor pressure drop of less than 2.0 kbar with a rapid temperature change, demonstrating cooling (+ minor decompression). In concurrence with textural data, this calculation helps in the reconstruction of the P-T path that the rock had traversed, uncovering a clockwise P-T evolutionary trajectory (Fig. 6a). Comparison of P-T trajectories from this study with the earlier reported path from the Sonapahar area is shown figure 6b.

Table 1. Representative analyses of garnet (12 oxygen basis) and cordierite (18 oxygen basis)

Oxides (wt%)	Garnet						Cordierite					
	R	M	C	C	M	R	M	M	C	C	M	M
SiO_2	38.35	38.31	37.86	38.77	38.97	38.41	50.26	50.12	49.94	50.34	49.91	50.14
TiO_2	0.28	0.01	0.00	0.00	0.01	0.00	0.22	0.22	0.23	0.25	0.23	0.24
Al_2O_3	20.92	21.24	20.87	20.79	21.55	21.21	32.53	32.93	31.90	31.84	31.58	31.87
Cr_2O_3	0.38	0.01	0.03	0.04	0.01	0.02	0.28	0.30	0.28	0.29	0.29	0.29
FeO	29.88	31.77	30.58	30.67	30.72	30.65	6.97	7.34	6.71	6.42	6.49	6.56
MnO	7.03	7.10	7.37	6.72	7.15	7.26	0.12	0.00	0.08	0.22	0.15	0.15
MgO	3.32	3.16	2.91	3.27	3.06	2.99	8.78	8.79	8.98	8.94	8.74	8.96
CaO	0.77	0.73	0.59	0.76	0.66	0.63	0.00	0.02	0.00	0.02	0.02	0.01
Na_2O	0.12	0.03	0.03	0.01	0.00	0.02	0.15	0.16	0.18	0.14	0.38	0.16
K_2O	0.02	0.02	0.00	0.02	0.02	0.01	0.00	0.00	0.02	0.00	0.00	0.01
Total	101.08	102.36	100.26	101.06	102.14	101.20	99.31	99.89	98.31	98.46	97.80	98.39
Si	3.04	3.02	3.04	3.07	3.05	3.05	5.09	5.05	5.10	5.13	5.12	5.11
Ti	0.02	0.00	0.00	0.00	0.00	0.00	0.02	0.02	0.02	0.02	0.02	0.02
Al	1.95	1.97	1.97	1.94	1.99	1.98	3.88	3.91	3.84	3.82	3.82	3.83
Cr	0.02	0.00	0.00	0.00	0.00	0.00	0.02	0.02	0.02	0.02	0.02	0.02
Fe^{3+}	0.00	0.01	0.00	0.00	0.00	0.00	0.05	0.05	0.07	0.07	0.07	0.07
Fe^{2+}	1.98	2.09	2.05	2.03	2.01	2.03	0.54	0.57	0.50	0.48	0.49	0.49
Mn	0.47	0.47	0.50	0.45	0.47	0.49	0.01	0.00	0.01	0.02	0.01	0.01
Mg	0.39	0.37	0.35	0.39	0.36	0.35	1.32	1.32	1.37	1.36	1.34	1.36
Ca	0.07	0.06	0.05	0.06	0.06	0.05	0.00	0.00	0.00	0.00	0.00	0.00
Na	0.02	0.00	0.01	0.00	0.00	0.00	0.03	0.03	0.04	0.03	0.07	0.03
K	0.00	0.00	0.00	0.00	0.00	0.00	0.00	0.00	0.00	0.00	0.00	0.00
Total	7.96	8.00	7.98	7.96	7.95	7.96	10.96	10.98	10.97	10.95	10.97	10.96
X_{Mg}	0.17	0.15	0.15	0.16	0.15	0.15	0.71	0.70	0.73	0.74	0.73	0.74

X_{Mg} = Mg/(Mg+Fe), C = Core, M = mantle R = rim.

4.d. Geothermobarometry

The foundation of the P-T calculation in the winTWQ computer program lies in the intersection of four distinct reactions within the P-T space. The thermodynamic data by Berman & Aranovich (1996, updated December 2006) are utilized in the winTWQ program. This dataset encompasses information about the end-member phases. Central to the winTWQ calculation are the end-member phases, each representing a distinct mineral composition. These include spinel, almandine, pyrope, cordierite, sillimanite, ilmenite, and beta-quartz. These minerals form the basis upon which the P-T conditions of the sample are inferred. These equilibria, which are formulated based on the selected end-member phases, reveal the geological evolution of the granulite. Each equilibrium compresses a unique mineralogical composition and offers a window into the conditions under which these minerals coexisted and transformed (Table. 4). Upon performing the calculations within the winTWQ program, a specific P-T condition emerged as the peak condition for the studied sample. The results indicate temperatures exceeding 950°C and pressures of approximately 8.8 kbar (Fig. 7).

The utilization of different conventional thermometers and barometers has yielded a range of outcomes (Table 5). By employing thermometric models such as those formulated by Vielzeuf (1983) and Perchuk (1991), based on the cordierite-spinel pair, temperature determinations have ranged from 850°C to 890°C and 879°C to 910°C, respectively. In the case of garnet–biotite pairs in the prograde stage, thermometer models, viz., Thompson (1976), Ferry & Spear (1978), Hodges & Spear (1982), Pigage & Greenwood (1982), Ganguly & Saxena (1984), and Williams & Grambling (1990), have yielded a broader range of temperatures, from 874°C to 1042°C. In the geobarometric models of Vielzeuf (1983) and Perchuk (1991), utilizing the peak assemblage spinel-cordierite-quartz gives a pressure range between 8.5 and 9.8 kbar. We have also utilized barometric models of Wells (1979), Aranovich and Podlesskii (1983, 1989), and Nichols *et al.* (1992) based on mineral assemblage Garnet–Cordierite–Sillimanite–Quartz and give us pressure in the range of 6.6 to 7.6 kbar. This divergence in pressure and temperature outputs across different conventional thermobarometric models is because of the distinct thermodynamic datasets that each model includes in its calculations.
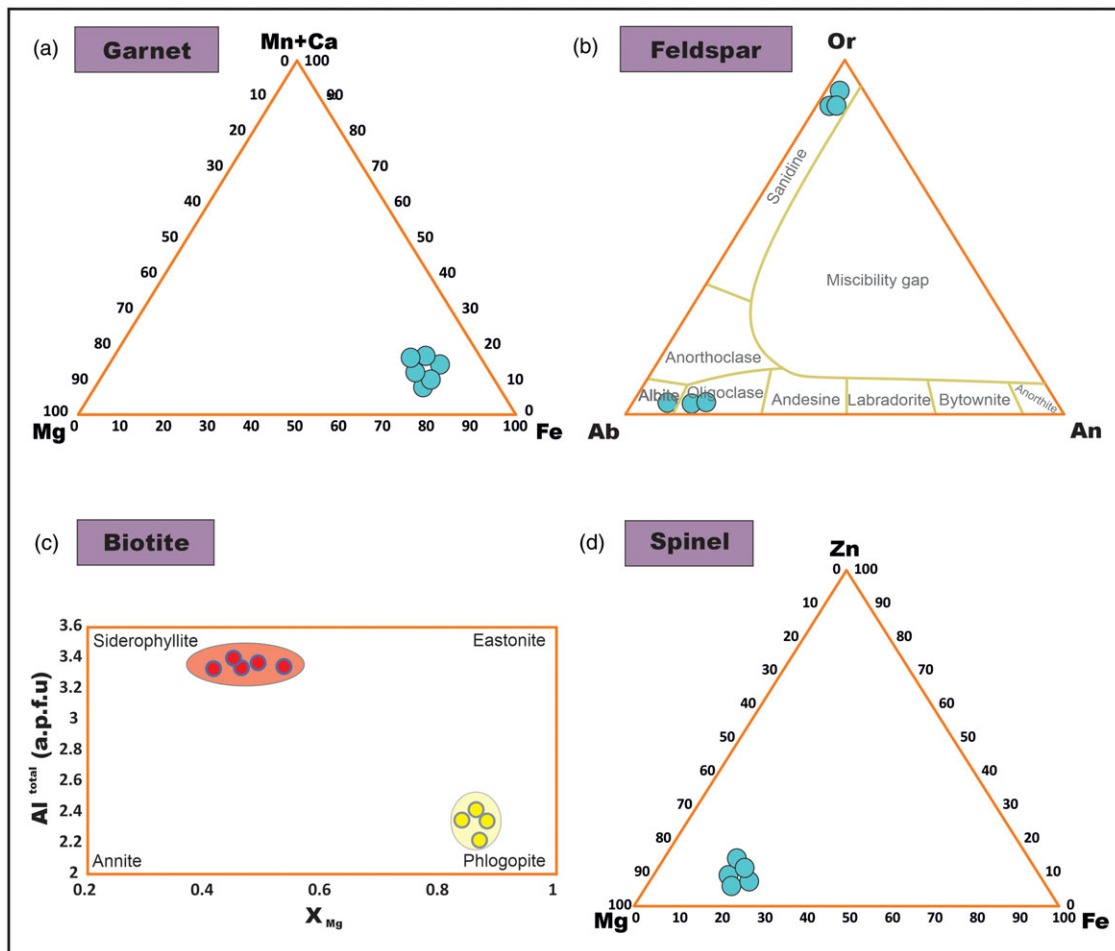
Figure 4. (a) Triangular plot of garnet showing Fe-rich (almandine) composition, (b) triangular plot of feldspar showing a higher concentration of sanidine and oligoclase composition, (c) X_{Mg} vs Al^{total} plot showing the composition of biotite, (d) triangular plot showing the composition of spinel.

4.e. Whole-rock geochemistry

Table 3 contains the major and trace element data for representative metapelite samples. Except for sample S2, which has noticeably higher SiO_2 (64.20 wt%) and MgO (6.46 wt%) contents, the samples have comparable SiO_2 (61.04–63.56 wt%) and MgO (5.31–7.99 wt%) contents. With A/CNK (CaO + Na_2O + K_2O) values of 1.64–3.08 and high levels of Al_2O_3 (15.28–17.11 wt%), all samples are peraluminous. Fe_2O_3 (6.37–7.06 wt%), FeO (0.71–0.78 wt%), CaO (0.85-0.18 wt%), and Na_2O (0.28–1.21 wt%) concentrations vary in the samples, whereas the concentration of K_2O (2.04–2.98 wt%) remains in close approximation. The samples contain Mg# values between 22.60 and 40.00 (Mg# = 100 MgO/ [MgO + FeO]). The samples are notably K_2O-rich and Na_2O-poor, with K_2O/Na_2O > 1.0 (1.56–8.22), showing that K-rich minerals are present in large amounts.

To understand the development of any geological region, it is essential to analyse its elemental composition at its current state. Metamorphic recrystallization is typically observed in closed systems due to diffusion-controlled chemical reactions in solid materials. To resolve this, we can correlate the levels of trace elements and REE in metamorphosed rocks with those found in chondrites and the primitive mantle. Figure 8a presents the rare earth elements (REEs) normalized to chondrites to offset the Oddo-Harkins effect. For the most part, the chondrite-normalized

REEs display a smooth trend in both the light rare earth elements (LREE) and heavy rare earth elements (HREE) groups, except for Europium (Eu). Besides samples S4 and S5, other samples show varied REE concentrations (279.17–366.06 ppm), fractionated REE patterns with $(La/Yb)N$ = 4.12–11.59 and negative Eu anomalies (Eu/Eu* = 0.37–0.98). The negative Eu anomaly is attributed to the early formation of plagioclase, as Eu^{2+} takes the place of Ca^{2+} in this feldspar. This peculiar anomaly may be linked to a reducing environment. Moreover, the cerium (Ce) anomaly is notably absent, as the graph illustrates a consistent increase in Ce content across all the samples. The range of the LREE/HREE ratios is 3.45 to 4.94. Furthermore, no correlations between REE levels and K2O or Al2O3 are seen, suggesting that the host minerals for REEs are probably accessory minerals rather than clay minerals (Gromet *et al.* 1984; Bhat and Ghosh, 2001). All samples are similar to the typical upper continental crust (UCC; Taylor and McLennan, 1995) in terms of their moderately fractionated chondrite-normalized REE patterns (Fig. 10a). The presence of LREE enrichment and negative Eu anomalies in metapelites are distinctive characteristics indicative of continental crust origins.

The multi-element primitive mantle pattern (spider diagram) (Fig. 8b) provides insights into the characteristics of source rock before metamorphism. In sedimentary contexts, the distribution of REEs serves as a highly accurate indicator of their origin (Taylor and McLennan. 1985). In Figure 8b, we observe a notable

Table 2. Representative analyses of Biotite (24 oxygen basis), feldspar (8 oxygen basis) and spinel (24 oxygen basis)

Biotite

Oxides (wt%)	I	I	I	S	S
SiO_2	35.81	35.27	35.77	41.35	40.30
TiO_2	0.01	1.74	3.26	1.32	1.64
Al_2O_3	17.80	17.72	17.16	13.41	14.14
FeO	18.97	16.18	20.06	5.10	6.42
MnO	0.10	0.00	0.12	0.10	0.05
MgO	9.06	10.67	8.01	22.75	21.50
CaO	0.00	0.00	0.09	0.04	0.03
Na_2O	0.00	0.18	0.19	1.14	0.94
K_2O	9.69	9.85	9.87	8.38	8.38
Cl	0.00	0.82	0.95	0.18	0.24
Total	90.93	91.78	94.82	93.14	93.01
Si	5.67	5.50	5.50	5.92	5.82
Al^{IV}	2.33	2.50	2.50	2.07	2.17
Al^{VI}	1.00	0.82	0.83	0.15	0.18
Ti	0.00	0.20	0.38	1.24	1.14
Fe^{2+}	2.51	2.11	2.58	0.63	0.80
Mn	0.01	0.00	0.02	0.01	0.00
Mg	2.14	2.48	1.84	4.82	4.59
Na	0.00	0.05	0.06	0.31	0.26
K	1.96	1.96	1.94	1.54	1.55
Cl	0.00	0.22	0.25	0.08	0.09
Total	15.64	15.63	15.65	16.73	16.55
X_{Mg}	0.46	0.54	0.42	0.86	0.83

Feldspar

Oxides	M	M	C	I	I
SiO_2	65.70	65.24	65.32	65.43	65.78
TiO_2	0.75	0.47	0.63	0.53	0.47
Al_2O_3	17.54	17.77	18.82	19.33	19.57
Cr_2O_3	0.39	0.37	0.31	0.27	0.22
FeO	0.00	0.00	0.00	0.01	0.00
MnO	0.00	0.01	0.00	0.00	0.00
MgO	0.05	0.00	0.00	0.00	0.01
CaO	0.05	0.08	0.05	3.38	2.67
Na_2O	0.47	0.95	0.69	9.51	9.73
K_2O	15.51	15.12	14.66	0.22	0.22
Total	100.27	99.48	100.11	98.45	98.38
Si	3.02	3.01	2.99	2.93	2.93
Ti	0.03	0.02	0.02	0.02	0.02
Al	0.95	0.97	1.01	1.02	1.03
Cr	0.01	0.01	0.01	0.01	0.01
Mn	0.00	0.00	0.00	0.00	0.00
Mg	0.00	0.00	0.00	0.00	0.00
Ca	0.00	0.00	0.00	0.16	0.13
Na	0.04	0.09	0.06	0.82	0.84
K	0.91	0.89	0.85	0.01	0.01
An	0.00	0.00	0.00	0.16	0.13
Ab	0.04	0.09	0.07	0.83	0.86
Or	0.95	0.91	0.93	0.01	0.01

Spinel

Oxides	M	M	M	M	M
SiO_2	0.02	0.03	0.04	0.03	0.03
TiO_2	0.02	0.01	0.01	0.01	0.01
Al_2O_3	65.06	65.35	65.30	64.45	63.68
Cr_2O_3	0.00	0.01	0.05	0.11	0.13
FeO	10.71	10.92	11.66	12.36	13.03
MnO	0.18	0.17	0.14	0.18	0.20
MgO	21.21	20.95	20.65	19.87	19.31
CaO	0.02	0.02	0.02	0.01	0.02
Na_2O	0.07	0.06	0.06	0.08	0.07
ZnO	1.97	1.67	1.37	1.64	2.14
Total	99.25	99.20	99.30	98.75	98.62
Si	0.00	0.01	0.01	0.01	0.01
Ti	0.00	0.00	0.00	0.00	0.00
Al	15.48	15.55	15.56	15.53	15.44
Cr	0.00	0.00	0.01	0.02	0.02
V	0.00	0.00	0.00	0.00	0.00
Fe^{2+}	1.30	1.42	1.55	1.67	1.72
Fe^{3+}	0.51	0.43	0.42	0.44	0.52
Mn	0.03	0.03	0.02	0.03	0.03
Mg	6.38	6.31	6.22	6.05	5.92
Ca	0.00	0.00	0.00	0.00	0.00
Zn	0.29	0.25	0.20	0.25	0.32
X_{Mg}	0.22	0.23	0.24	0.26	0.27

X_{Mg} = Mg/(Mg+Fe), X_{Fe} = Fe/(Fe+Mg), G = groundmass, I = inclusion, S = symplectite, C = Core, M = mantle.

Figure 5. (a) P-T pseudosection calculated for the spinel + quartz bearing Mg-Al bearing granulite in the model system $MnO-Na_2O-CaO-K_2O-FeO-MgO-Al_2O_3-SiO_2-H_2O-TiO_2-Fe_2O_3$ (MnNCKFMASHTO), b) distribution of the calculated modal isopleths of different minerals for the calculated pseudosection: biotite (Bt), cordierite (Crd), spinel (Spl) and garnet (Grt).

Figure 6. (a) Distribution of the calculated X_{Mg} [= Mg/ (Mg+ Fe)] isopleths for biotite, cordierite, spinel and garnet for the calculated pseudosection. The inferred cooling (+ minor decompression) P–T path is indicated by a black arrow and (b) comparison of metamorphic P-T evolution path from Sonapahar, SMGC. Metamorphic boundaries displayed in the background are modified after Vernon and Clarke (2008).

enrichment of large-ion-lithophile elements, specifically Rb, Ba, and Pb, alongside the depletion of high-field-strength elements such as Nb and Ta. These particular geochemical signatures are indicative of primary rock sources that fall within the intermediate-felsic category (Zhao *et al.* 2018). Notably, the presence of a

conspicuously Ti-negative peak can be attributed to the non-involvement of any magmatic and partial melting processes in the formation of protolith, which took place under conditions characterized by a low oxygen fugacity. Furthermore, to account for the presence of minerals such as rutile and ilmenite, the
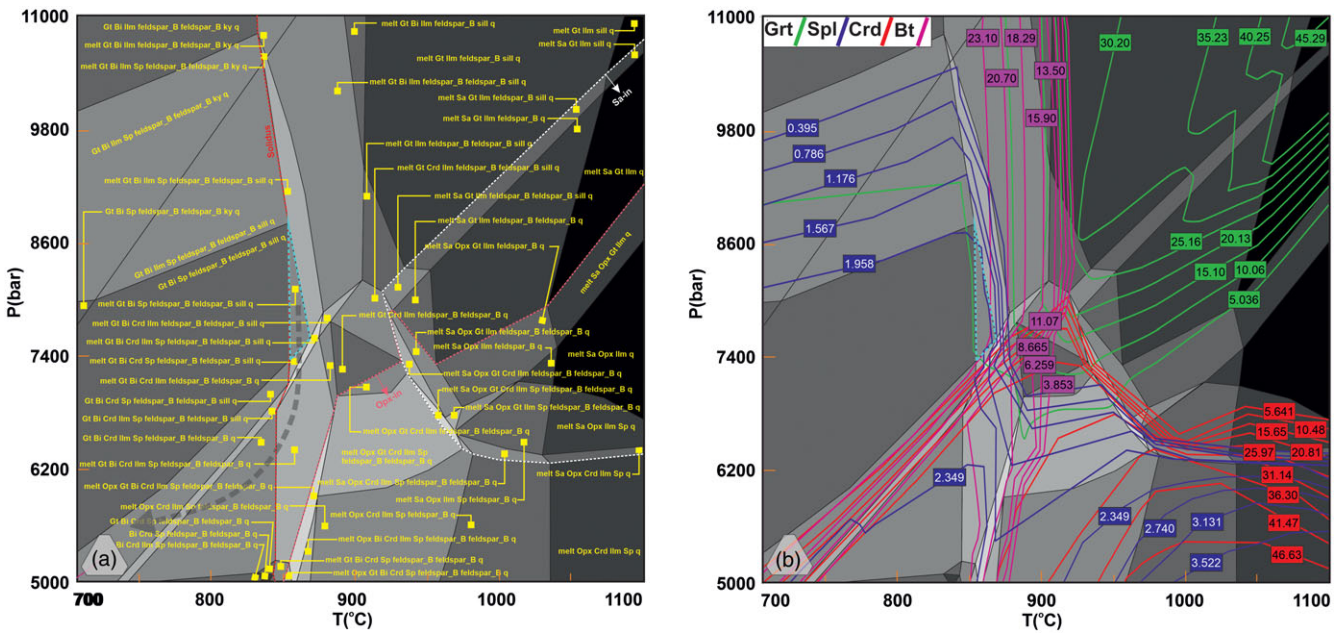
Table 3. Whole rock geochemistry of the pelitic granulite, major oxide (wt %), trace element and REE (ppm) (Sn-7F)

Sample No.	Sn-7F (1)	Sn-7F (2)	Sn-7F (3)	Sn-7F (4)	Sn-7F (5)	Sn-7F (6)	Sn-7F (7)	Sn-7F (8)	Sn-7F (9)	Sn-7F (10)	Sn-7F (11)	Sn-7F (12)	Sn-7F (13)	Sn-7F (14)	Sn-7F (15)	Sn-7F (16)	Sn-7F (17)	Sn-7F (18)	Sn-7F (19)	Sn-7F (20)
Weight Percent (%)																				
SiO_2	63.56	64.20	61.04	62.79	61.19	63.04	62.16	62.64	63.88	61.92	62.12	62.40	62.93	62.34	62.89	62.14	62.62	61.12	63.62	62.58
TiO	1.02	0.89	0.62	0.42	0.72	0.67	0.68	0.72	0.96	0.52	0.70	0.70	0.84	0.60	0.79	0.64	0.76	0.67	0.78	0.72
Al_2O_3	16.20	15.28	17.02	16.92	17.11	15.88	16.69	16.40	15.74	16.97	16.50	16.55	16.17	16.64	16.28	16.67	16.15	17.07	15.58	16.44
Fe_2O_3	6.44	7.06	6.70	6.37	6.38	6.46	6.58	6.57	6.75	6.53	6.42	6.57	6.73	6.40	6.63	6.51	6.88	6.54	6.76	6.57
FeO	0.72	0.78	0.74	0.71	0.71	0.72	0.73	0.73	0.75	0.73	0.71	0.73	0.75	0.71	0.74	0.72	0.76	0.73	0.75	0.73
MnO	0.12	0.10	0.08	0.10	0.11	0.10	0.10	0.10	0.11	0.09	0.11	0.10	0.10	0.10	0.10	0.10	0.09	0.10	0.10	0.10
MgO	7.24	6.46	7.99	6.44	7.09	6.91	5.31	7.02	6.85	7.22	7.00	6.17	7.23	6.81	6.39	6.79	7.23	7.54	6.69	6.81
CaO	0.18	0.20	0.61	0.56	0.85	0.82	0.74	0.54	0.19	0.59	0.84	0.64	0.33	0.74	0.49	0.69	0.41	0.73	0.51	0.56
Na_2O	0.28	0.38	0.39	1.21	0.88	0.72	1.12	0.64	0.33	0.80	0.80	0.88	0.35	0.94	0.70	0.83	0.39	0.64	0.55	0.70
K_2O	2.74	2.82	2.13	2.04	2.89	2.98	3.45	2.60	2.78	2.09	2.94	3.03	2.56	2.64	2.94	2.68	2.48	2.51	2.90	2.71
P_2O_5	0.03	0.06	0.07	0.07	0.06	0.09	0.07	0.06	0.05	0.07	0.08	0.07	0.05	0.07	0.06	0.07	0.07	0.07	0.08	0.06
LOI	0.83	1.44	1.33	0.86	1.12	0.83	0.89	1.07	1.14	1.10	0.98	0.98	1.20	0.94	1.03	1.02	1.39	1.23	1.14	1.05
Total	**99.36**	**99.67**	**98.72**	**98.49**	**99.11**	**99.22**	**98.52**	**99.10**	**99.52**	**98.61**	**99.17**	**98.81**	**99.25**	**98.94**	**99.04**	**98.86**	**99.20**	**98.92**	**99.45**	**99.02**
Parts per million (ppm)																				
La	62.000	66.000	70.000	52.000	61.000	79.000	67.170	65.000	64.000	61.000	70.000	66.085	66.000	64.000	65.390	65.695	68.000	65.500	72.500	65.271
Ce	122.00	120.00	182.00	119.00	125.00	144.00	143.67	135.33	121.00	150.50	134.50	139.50	141.33	129.33	133.33	141.50	151.00	153.50	132.00	136.37
Pr	18.000	18.270	15.010	19.120	18.660	22.060	16.400	18.520	18.135	17.065	20.360	17.460	17.093	19.947	17.685	18.295	16.640	16.835	20.165	18.255
Nd	72.810	62.220	62.010	58.000	50.650	71.200	60.670	62.815	67.515	60.005	60.925	61.743	65.680	59.950	63.667	60.891	62.115	56.330	66.710	62.547
Sm	9.960	10.320	9.250	8.220	11.120	12.200	10.810	10.178	10.140	8.735	11.660	10.494	9.843	10.513	10.376	10.296	9.785	10.185	11.260	10.257
Eu	1.660	1.280	1.540	1.320	1.560	1.440	1.570	1.467	1.470	1.430	1.500	1.518	1.493	1.440	1.502	1.483	1.410	1.550	1.360	1.480
Gd	10.340	9.670	12.880	9.220	8.020	10.420	10.380	10.092	10.005	11.050	9.220	10.236	10.963	9.220	10.159	10.169	11.275	10.450	10.045	10.128
Tb	1.200	1.430	1.380	1.120	0.980	1.010	1.270	1.187	1.315	1.250	0.995	1.228	1.337	1.037	1.257	1.158	1.405	1.180	1.220	1.197
Dy	6.190	5.320	7.530	6.380	4.480	6.810	5.560	6.118	5.755	6.955	5.645	5.839	6.347	5.890	5.811	6.146	6.425	6.005	6.065	6.049
Ho	0.980	0.920	1.020	0.880	0.920	0.970	0.860	0.948	0.950	0.950	0.945	0.904	0.973	0.923	0.919	0.933	0.970	0.970	0.945	0.937
Er	1.920	1.740	1.760	1.740	1.820	1.980	1.980	1.827	1.830	1.750	1.900	1.903	1.807	1.847	1.879	1.851	1.750	1.790	1.860	1.846
Tm	0.180	0.220	0.180	0.280	0.220	0.300	0.250	0.230	0.200	0.230	0.260	0.240	0.193	0.267	0.227	0.243	0.200	0.200	0.260	0.233
Yb	1.640	1.260	1.350	1.710	1.820	1.990	1.600	1.628	1.450	1.530	1.905	1.614	1.417	1.840	1.559	1.683	1.305	1.585	1.625	1.625
Lu	0.240	0.150	0.150	0.180	0.440	0.230	0.250	0.232	0.195	0.165	0.335	0.241	0.180	0.283	0.226	0.247	0.150	0.295	0.190	0.234
Y	28.000	22.000	32.000	18.000	23.000	26.000	23.480	24.833	25.000	25.000	24.500	24.157	27.333	22.333	24.438	24.552	27.000	27.500	24.000	24.664
Sc	13.000	14.000	18.000	13.000	16.000	17.050	15.010	15.175	13.500	15.500	16.525	15.093	15.000	15.350	14.562	15.706	16.000	17.000	15.525	15.154
P	270.00	220.00	210.00	110.00	220.00	380.00	250.00	250.00	245.00	160.00	300.00	250.00	233.33	236.66	248.33	236.66	215.00	215.00	300.00	238.75
Al	8.380	8.660	7.730	3.420	7.700	8.640	7.200	6.840	8.520	5.575	8.170	7.020	8.257	6.587	7.520	6.922	8.195	7.715	8.650	7.321
Na	0.306	0.390	0.299	0.157	0.306	0.515	0.258	0.274	0.348	0.228	0.411	0.266	0.332	0.326	0.293	0.302	0.345	0.303	0.453	0.313

Table 3. (*Continued*)

Sample No.	Sn-7F (1)	Sn-7F (2)	Sn-7F (3)	Sn-7F (4)	Sn-7F (5)	Sn-7F (6)	Sn-7F (7)	Sn-7F (8)	Sn-7F (9)	Sn-7F (10)	Sn-7F (11)	Sn-7F (12)	Sn-7F (13)	Sn-7F (14)	Sn-7F (15)	Sn-7F (16)	Sn-7F (17)	Sn-7F (18)	Sn-7F (19)	Sn-7F (20)
Mg	1.500	1.340	1.290	0.830	1.330	1.110	1.290	1.180	1.420	1.060	1.220	1.235	1.377	1.090	1.297	1.172	1.315	1.310	1.225	1.234
Cu	122.42	100.88	102.00	98.250	66.800	88.720	97.000	96.512	111.65	100.12	77.760	96.756	108.43	84.590	101.72	91.547	101.44	84.400	94.800	96.573
Co	15.880	17.980	13.230	14.440	13.860	15.010	16.500	15.067	16.930	13.835	14.435	15.783	15.697	14.437	16.166	14.684	15.605	13.545	16.495	15.246
Ni	40.230	32.810	31.540	36.880	34.820	34.900	34.180	35.197	36.520	34.210	34.860	34.688	34.860	35.533	35.299	34.586	32.175	33.180	33.855	35.070
Zn	106.200	102.600	184.900	198.100	184.400	188.700	196.900	160.817	104.400	191.500	186.550	178.858	131.233	190.400	154.039	185.636	143.750	184.650	145.650	165.327
Rb	176.200	164.080	182.430	180.820	185.320	191.070	163.050	179.987	170.140	181.625	188.195	171.518	174.237	185.737	171.059	180.446	173.255	183.875	177.575	177.870
Li	28.900	18.200	17.400	16.100	17.900	8.100	11.300	10.500	23.550	16.750	13.000	10.900	21.500	14.033	15.117	13.550	17.800	17.650	13.150	16.050
Cr	62.000	88.000	82.000	96.000	106.000	110.000	91.330	90.667	75.000	89.000	108.000	90.998	77.333	104.000	85.666	95.999	85.000	94.000	99.000	90.750
Hf	4.890	4.470	6.385	3.890	4.915	6.855	3.420	4.975	4.680	5.138	5.885	4.198	5.248	5.220	4.358	5.073	5.428	5.650	5.663	4.975
Ta	0.900	0.900	1.000	0.800	1.000	1.000	0.900	0.900	0.900	0.900	1.000	0.900	0.933	0.933	0.900	0.933	0.950	1.000	0.950	0.925
Nb	6.760	10.220	8.280	9.860	9.450	8.210	8.720	8.797	8.490	9.070	8.830	8.758	8.420	9.173	8.669	8.886	9.250	8.865	9.215	8.787
Th	21.410	24.220	23.980	21.670	21.440	22.840	23.580	22.593	22.815	22.825	22.140	23.087	23.203	21.983	22.996	22.684	24.100	22.710	23.530	22.717
Sr	66.410	48.200	62.880	58.900	64.460	94.640	63.330	65.915	57.305	60.890	79.550	64.623	59.163	72.667	62.183	68.354	55.540	63.670	71.420	65.592
Mo	0.640	0.625	0.657	0.593	0.625	0.633	0.641	0.630	0.633	0.625	0.629	0.635	0.641	0.617	0.634	0.630	0.641	0.641	0.629	0.630
Pb	32.500	40.880	26.080	40.100	29.800	32.240	29.820	33.600	36.690	33.090	31.020	31.710	33.153	34.047	33.370	31.940	33.480	27.940	36.560	33.128
V	66.000	82.000	64.000	61.000	58.000	68.000	65.330	66.500	74.000	62.500	63.000	65.915	70.667	62.333	68.610	63.805	73.000	61.000	75.000	66.354
Ba	480.000	520.000	580.000	548.000	520.000	440.000	532.830	514.667	500.000	564.000	480.000	523.748	526.667	502.667	515.832	522.583	550.000	550.000	480.000	516.937
Zr	188.000	142.000	170.000	152.00	181.00	148.00	177.67	163.50	165.00	161.00	164.50	170.58	166.66	160.33	168.72	165.36	156.00	175.50	145.00	165.27
Sn	0.200	0.300	0.200	0.100	0.500	0.300	0.200	0.300	0.250	0.150	0.400	0.250	0.233	0.300	0.250	0.267	0.250	0.350	0.300	0.263
Y	28.000	22.000	32.000	18.000	23.000	26.000	23.480	24.833	25.000	25.000	24.500	24.157	27.333	22.333	24.438	24.552	27.000	27.500	24.000	24.664
Cs	1.525	1.060	2.030	1.473	0.983	1.267	1.521	1.408	1.293	1.752	1.125	1.465	1.538	1.241	1.407	1.447	1.545	1.507	1.163	1.408
Ga	24.510	26.810	25.170	11.810	21.950	22.190	21.290	20.960	25.660	18.490	22.070	21.125	25.497	18.650	22.637	20.562	25.990	23.560	24.500	21.836
In	0.080	0.080	0.080	0.050	0.080	0.080	0.070	0.070	0.080	0.065	0.080	0.070	0.080	0.070	0.073	0.072	0.080	0.080	0.080	0.074
Tl	0.740	0.760	0.920	0.390	0.510	1.040	0.630	0.660	0.750	0.655	0.775	0.645	0.807	0.647	0.680	0.692	0.840	0.715	0.900	0.706
Cd	0.205	0.213	0.125	0.133	0.163	0.173	0.157	0.167	0.209	0.129	0.168	0.162	0.181	0.157	0.178	0.153	0.169	0.144	0.193	0.167
As	1.600	0.900	0.000	0.300	0.300	0.200	0.300	0.300	1.250	0.150	0.250	0.300	0.833	0.267	0.617	0.233	0.450	0.150	0.550	0.488
U	2.450	2.220	2.210	2.870	2.980	3.450	3.080	2.697	2.335	2.540	3.215	2.888	2.293	3.100	2.704	2.881	2.215	2.595	2.835	2.745

Table 4. P–T calculation at peak stage using winTWQ (version 2.34) program

Serial no.	Equilibria plotted	S (joule/mol)	V (joule/bar)
The P–T condition obtained by specific equilibria for peak stage			
1	2 Si + Py = 5 bQz + 3 Spl	−1.33	−2.43
2	2 Alm + 15 bQz + 6 Spl = 2 Py + 3 fCd	112.54	14.59
3	4 Si + 5 bQz + 2 Alm= 3 fCd	−141.21	−15.22
4	6 Si + Py + 2 Alm = 3 fCd + 3 Spl	−129.85	−17.92
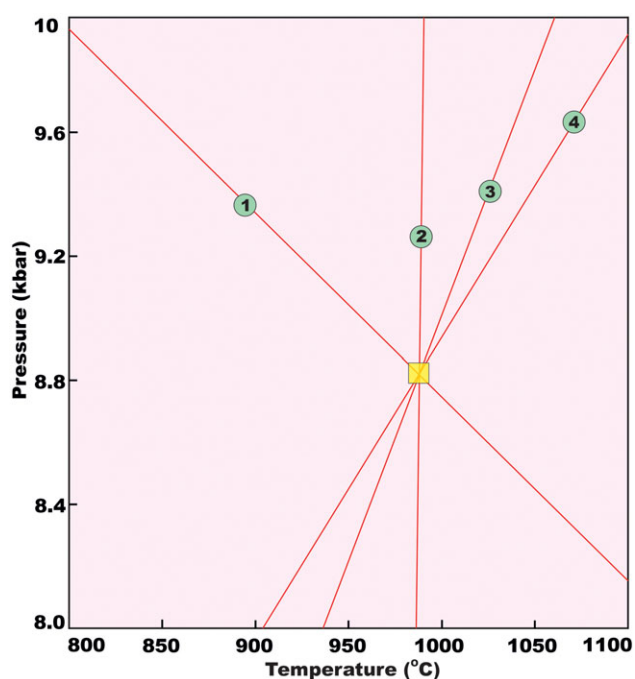
Figure 7. Results of the simultaneous calculations of pressure (P) and temperature (T) obtained using the winTWQ program.

composition contains substantial amounts of TiO2, up to 1.00 wt.%. In primitive-mantle-normalized trace element diagrams, the samples show positive anomalies for Pb but negative anomalies for Ta, Nb, Sr, P and Ti (Fig. 10b). The negative correlation between Nb-Ta and Zr-Hf indicated that the geochemical behaviour of these two pairs of elements was identical and moderately affected by weathering and sediment deposition. Th and U show a positive association, and the Th/U ratio ranges from 9.62 to 11.90, which is much higher than the upper crust's typical Th/U ratio of 3.8 (Taylor and McLennan, 1985). This suggests that the source region has undergone moderate weathering.

The data for the samples mostly plot in the clay rock and greywacke, intermediate and alkaline volcanic-greywacke, and their overlapped areas, according to the A-C-FM ternary discrimination diagram (Fig. 9a; secondary source after Wang *et al.* 1987). The majority of the data were plotted in the argillaceous sedimentary rock field in the (al + fm)-(c + alk)-Si diagram (Fig. 9b; Simonen, 1953). The sample data are plotted in the shale, iron shale, and greywacke fields of the log (Fe_2O_3/K_2O)- log (SiO_2/Al_2O_3) diagram (Fig. 9c; Herron, 1988). The shale, clay

rock, and sandstone fields show the majority of the data on the La/Yb-REE plot (Fig. 9d; Gromet *et al.* 1984). Thus, it can be inferred that the protoliths of the studied samples from the Sonapahar region were clay rocks and sandstones.

4.f. Weathering of the source area and sediment sorting

According to (McLennan 1993; Panahi *et al.* 2000), the chemical index of alteration (CIA), first suggested by Nesbitt and Young (1982), is computed as CIA = Al_2O_3/[Al_2O_3 + CaO* + Na_2O + K_2O] 100 (in molar proportions). CaO* is the CaO linked with the silicate percentage of the sample. This metric has been used extensively to gauge the severity of source weathering. Indicating a reasonably high level of weathering, the CIA values of the examined samples range from 75.86 to 84.46 (average = 80.63).

The K_2O/Na_2O and SiO_2/Al_2O_3 ratios can frequently be used to determine the degree of weathering and age of source rock (Roser and Korsch, 1986; Wei *et al.* 2009). The K2O/Na2O ratios of the samples under study range from 0.63 to 8.22 (average: 3.90), indicating that K was retained in the protolith deposits while Na was lost due to weathering and leaching. The SiO_2/Al_2O_3 ratios of the examined samples range from 2.24 to 4.61 (average = 3.26), indicating that the protolith sediments were deposited close to the source and had a low degree of maturity. The index of compositional variability (ICV = [Na2O + K2O + CaO + MgO + MnO + Fe2O3t + TiO2]/Al2O3) determines the amount of alumina relative to other major cations and the compositional maturity of a rock or mineral (Cox *et al.* 1995; Van de Kamp and Leake, 1985; Weaver, 1989). The majority of the samples under examination have an average ICV of 1.29 (1.09–1.68), suggesting that they may have originated from a tectonically active environment.

The degree of weathering of the studied samples is significantly higher than that of typical shales, as shown in the Al2O3-(CaO* + Na2O)-K2O ternary diagram (Fig. 10a; Fedo *et al.* 1995), indicating that plagioclase was weathered into clay minerals (LaMaskin *et al.* 2008). Most data plots around the top crustal field in the Th/Sc-Zr/Sc diagram (Fig. 10b; McLennan, 1993) depict the degree of sedimentary sorting and recycling (Asiedu *et al.* 2000). According to Li *et al.* (2005), recycled sediments show a greater rise in Zr/Sc than Th/Sc, indicating that they are directly derived from igneous rocks. The relationship between Th and Zr (Fig. 10b) indicates that neither Th nor Zr was extremely mobile during metamorphism (McLennan, 1993; Yang *et al.* 1998). Sorting processes can be seen in an Al-Ti-Zr ternary graphic. While sediments with a small range of TiO2-Zr values suggest immature compositions, sediments with a large range of values show better compositional maturity (Garcia *et al.* 1994). With a few notable outliers, the limited range of TiO2-Zr values in the analyzed samples suggests poor sorting and rapid sediment deposition (Fig. 10c).

4.g. Provenance and depositional settings

The original compositions of the source rocks can also be constrained using the Al_2O_3-(CaO* + Na_2O)-K_2O ternary diagram (Fig. 10a; Fedo *et al.* 1995). Since the weathering trajectories for the sedimentary rocks are parallel to the A-CN line, it is possible to deduce the source composition by extending the data backwards to the feldspar junction (Nesbitt and Young, 1984, 1989). The majority of the studied samples form an array that intersects the feldspar join at a point that suggests the source had a plagioclase: K-feldspar ratio of less than 3:1, a characteristic

Table 5. Average temperature and pressure obtained using different geothermobarometer

Sl. no.	Models	Average temperature/pressure
Temperature (°C)		
A	**Cordierite–spinel**	
1	Vielzeuf (1983)	850 – 890 °C
2	Perchuk (1991)	87 – 910 °C
B	**Garnet–biotite**	
1	Thompson (1976)	885 – 960 °C
2	Ferry & Spear (1978)	880 – 940 °C
3	Hodges and Spear (1982)	874 – 980 °C
4	Pigage & Greenwood (1982)	920 – 1042 °C
5	Ganguly & Saxena (1984)	890 – 930 °C
6	Williams & Grambling (1990)	910 – 928 °C
Pressure (kbar)		
A	**Spinel–cordierite–quartz**	
1	Vielzeuf (1983)	7.8 – 8.8
2	Perchuk (1991)	8.6 – 9.8
B	**Garnet–Cordierite–Sillimanite–Quartz**	
1	Wells (1979)	6.8 – 7.4
2	Aranovich and Podlesskii (1983, 1989)	7.2 – 7.6
3	Nichols *et al.* (1992)	6.6 – 6.8

commonly found in granite and A-type granite. It appears that some samples (Fig. 10a; Fedo *et al.* 1995) are weathering products of granodiorite and tonalite.

The La/Th-Hf plot and discrimination diagrams for sandstone and mudstone are more accurate indicators of the source lithology for clastic deposits (Fig. 10d; Floyd and Leveridge, 1987; Roser and Korsch, 1988). The majority of the results show correlations with a felsic provenance and a tendency towards older sediment components in the analyzed samples. Data for nearly all samples plot in the intermediate-acid area of the Rb-K_2O plot (Floyd and Leveridge, 1987) (Fig. 10e). This shows that the samples being studied had a lithology that was predominately composed of felsic source rocks.

Immobile trace elements such as Th, Sc, Zr, and La are stable and insoluble, making them useful for provenance investigations (Bhatia, 1984; Bhatia and Crook, 1986). The most helpful plots for tectonic discrimination (Bhatia and Crook, 1986) employ the immobile trace elements La-Th-Sc and Th-Sc-Zr/10. The data for all sample plot within the field of the continental island arc (Fig. 10f and 10g).

The binary plot relating K/Rb and Rb/Sr ratios (Fig. 11a) (Abdel-Rahman and El-Kibbi 2001) serves as a tectonic discrimination diagram, elucidating the orogenic aspects of the tectonic evolution. Beyond these geochemical parameters, the SiO_2/ Rb/Zr ratio plot (Fig. 11b) by Harris *et al.* (1986) illustrates magmatic processes following a collision. The majority of sediment samples are positioned within the oceanic island arc (Field A) with some contributions from continental island arcs (Field B). This finding is supported by Figure 11c, where the La/Th ratio

exceeds one for all plotted samples, aligning with the tectonic environments detailed in Bhatia (1983 and 1985) and Bhatia and Crook (1986). Examining Table 4, the compositional estimates for the studied area align with those proposed by McLennan *et al.* (1980) and Taylor & McLennan (1985), highlighting their resemblance to Proterozoic sedimentary rock.

4.h. K-Ar Geochronology

Fundamentally, K-Ar dating is based on the natural decay process of the potassium isotope ^{40}K, which transforms into the argon isotope ^{40}Ar. The "age" deduced through K-Ar techniques essentially reflects the time passed since the formation of radiogenic argon by the decay of ^{40}K, and its subsequent entrapment within minerals or rocks. This chronometric insight can offer valuable information about cooling events related to the exhumation of metamorphic rock, a phenomenon (Kelley 2002).

The K-Ar ages of biotite obtained from the symplectite of Mg-Al granulite range from 432 to 456 Ma with ±1 sd. The comprehensive analytical data are detailed in Table 6. Notably, the isotopic data derived from biotite grains indicate an early Devonian metamorphic cooling event for the Sonapahar region. This significant event is dated at approximately weighted mean age 442.95 ± 3.64 Ma, as described in both Fig. 12 and Table 5.

4.i. Monazite Geochronology

Following systematic electron microprobe-backscatter electron (EPMA-BSE) imaging, sample (Sn-7F) with monazites having a uniform mineral composition and grain sizes ranging from 50 to 150 microns is selected for microprobe dating (Fig. 13). In the BSE pictures, the monazite grains exhibit uniform compositional zones. Monazite grains come in a variety of shapes, including anhedral, subhedral and spherical, and range in size from tiny (30–80 micrometres) to big (80–150 micrometres). They can be found in garnet's matrix and as inclusions. Monazite grains, which are found in garnet porphyroblasts, show a comparable yttrium (Y) structure from the rim to the core. The partitioning of Y in monazite is closely connected to the growth or consumption of peritectic garnet (Spear & Pyle, 2010; Bhowmik *et al.* 2014). The variation in the Y values in Table 6 corresponds to different monazite grains and links to different textural positions.

The data acquired after following conventional techniques for systematic EPMA dating demonstrate two unique sets of ages. Table 7 shows that the calculated ages correspond to 623 Ma–744 Ma and 1428 Ma–1637 Ma with ±2sd. Based on the data of the monazite grains, a recent metamorphic event in the Sonapahar area has been dated at a weighted mean age of 682.20 ± 28 Ma, whereas the inherited weighted mean age is considered around 1527.4 ± 38 Ma (Fig. 14). Figure 14a shows the probability density peaks of monazite ages from several spot sites. The plot (Fig. 14b) aids in restricting a probable age of the metamorphic event, as well as the graphical distribution of all estimated ages taking into account their error values. The results obtained from the monazite geochronology in this study indicate that the existing structure of the granulite in the Sonapahar region is the result of extensive reworking during the Neo-Proterozoic (682.20 ± 28 Ma) tectonothermal event.

5. Discussion

The results of this study provide light on the metamorphic evolution of the Mg-Al granulite found in Sonapahar, SMGC. A thorough understanding of the geological history is established
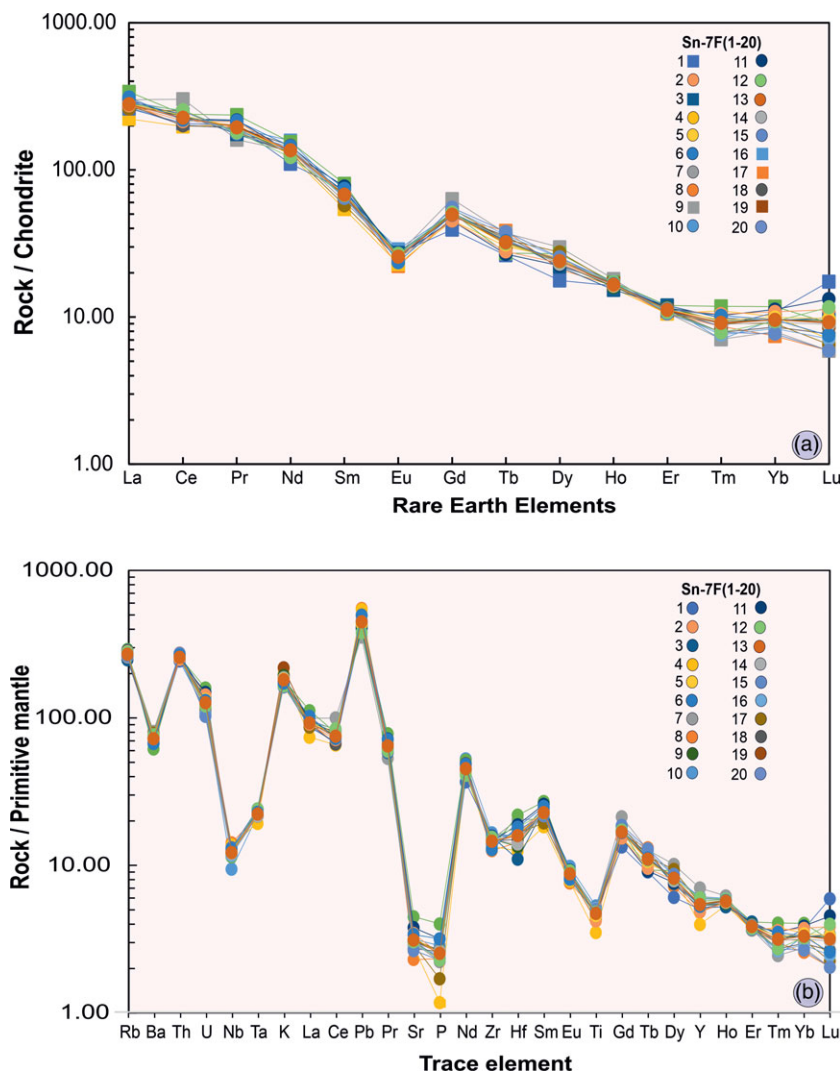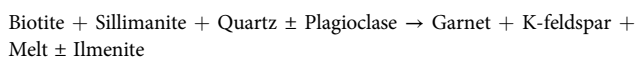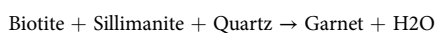
Figure 8. (a) Chondrite-normalised REE pattern for the pelitic granulites; (b) multi-element spider diagram normalized by the primitive mantle.

using an extensive approach that includes petrographic investigation, mineral chemistry, P-T pseudosection modelling, geochemistry, and geochronological estimation.

## 5.a. Textural relations and metamorphic reactions

In terms of petrological interpretations, the observed textures reveal crucial information about the early stages of dehydration reactions. Garnet porphyroblast containing inclusions of quartz, flaky biotite and acicular sillimanite suggests early-stage dehydration reactions during the prograde stage. This is demonstrated by the presence of garnet porphyroblast (Fig. 3a and 3b). The prograde reaction is marked by the following reactions:

Biotite + Sillimanite + Quartz → Garnet + H_2O

Biotite + Sillimanite + Quartz ± Plagioclase → Garnet + K-feldspar + Melt ± Ilmenite

In the [SiO_2-$6K_2O$]-[MgO+FeO]-[(Al_2O_3+Cr_2O_3+Fe_2O_3)-K_2O] diagram (Fig. 15), within the three-phase field of biotite–sillimanite–quartz, the analyzed garnet composition substantiates the aforementioned reactions. These reactions depict the discontinuous terminal nature of the metamorphic dehydration phase.

In the peak metamorphic stage, the combination of spinel and quartz alongside sillimanite assumes significant importance. This assemblage may form through a process wherein sillimanite and garnet are consumed to form spinel and quartz. For an assemblage to be categorized as UHT, it must exhibit spinel and quartz in direct contact (Zhang *et al.* 2012). Although Qz + Sp is often found in UHT terranes and may be suggestive of UHT conditions, its presence alone should probably not be used as a diagnostic indicator of UHT conditions, as the stability of spinel is strongly affected by minor components such as Zn and Cr (Kelsey and Hand, 2015 Harley, 2020). This distinctive reaction texture is frequently observed in our samples (as shown in Fig. 3c and 3d). Therefore, the fundamental reaction used to infer peak metamorphism in the studied rock is

Sillimanite + Garnet → Spinel + Quartz
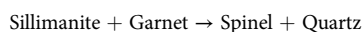
The presence of a symplectite structure consisting of biotite along with associated sillimanite and quartz suggests a probable reaction during the retrograde phase involving the transformation of garnet into secondary biotite (Fig. 3e and 3f). The conceivable reaction is

Garnet + melt → Biotite + Sillimanite + Quartz
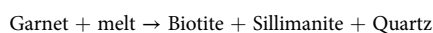
The presence of cordierite adjacent to biotite, sillimanite and quartz symplectites in the garnet-absent zone points to additional retrograde reactions or a cooling phase.
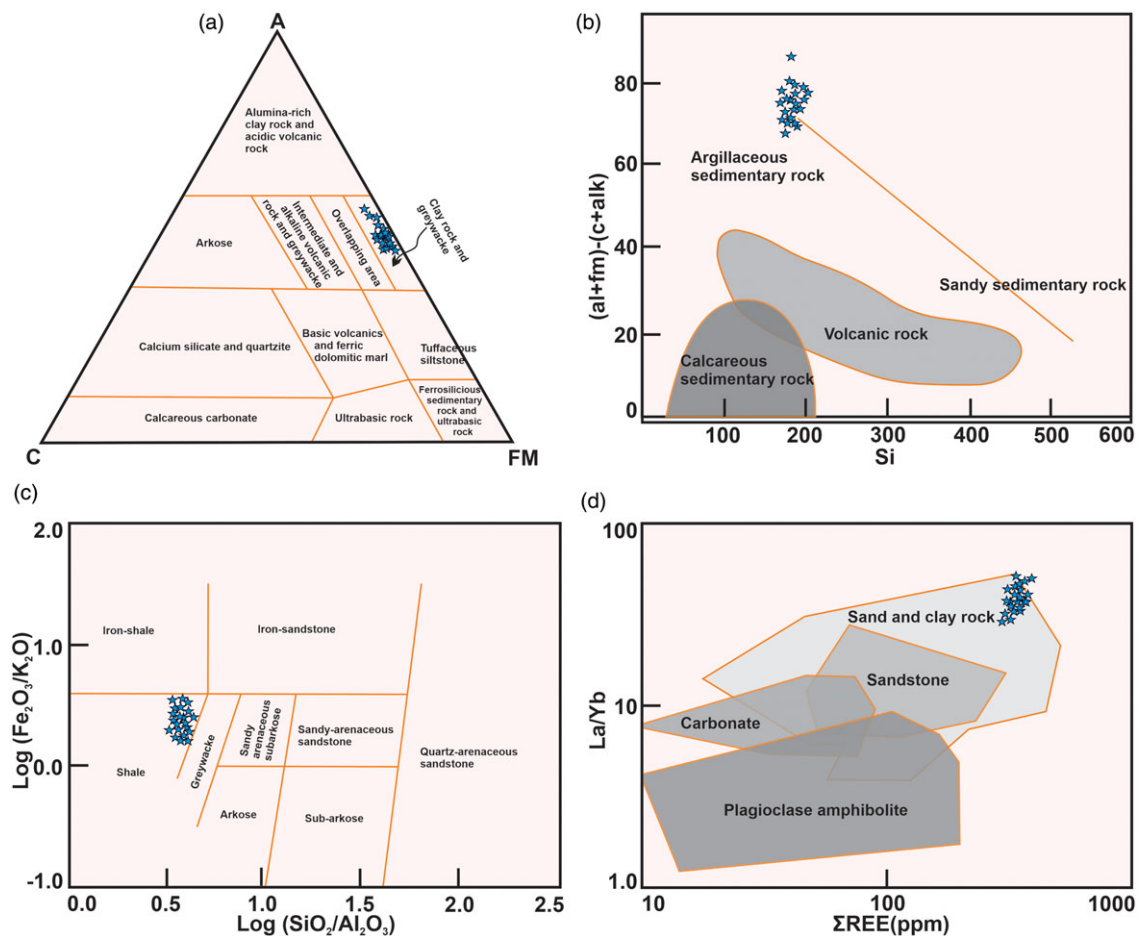
Figure 9. Classification diagrams of the samples in the Sonapahar area. (a) Ternary plot of A-C-FM (secondary source after Wang *et al.* 1987); (b) (al + fm)-(c + alk)-Si diagram (Simonen, 1953); (c) Log(Fe₂O₃/K₂O)-Log(SiO₂/Al₂O₃) diagram (Herron, 1988); (d) La/Yb-ΣREE diagram (Gromet *et al.* 1984).

5.b. P-T evolution

The integration of petrographic analysis with P-T pseudosection modelling and thermodynamic data implies a clockwise P-T trajectory for the granulitic terrane's evolution. This trajectory could be attributed to collisional tectonic activities resulting in crustal thickening. The P-T pseudosection approximations yielding < 2.0 kbars of decompression with rapid decrease in temperature indicate exhumation of lower crustal rocks from the granulite facies. Based on the texture of late-stage hydration reactions, the evidence suggests rapid cooling following minute decompression. The peak of metamorphic conditions is indicated by the presence of spinel and quartz exhibiting grain boundary sharing. This notion aligns well with the peak metamorphic conditions as suggested by the winTWQ software and conventional thermobarometry. These techniques converge to propose peak temperatures exceeding 900°C and pressures of around 8 kbars. Whereas in the case of pseudosection modelling observed peak mineral assemblage is found to occur at a temperature of around 870°C. Symplectite textures, a characteristic feature of imperfect or partially progressing metamorphic reactions due to decompression, also play an important role. Such textures are valuable in classifying granulite terranes and can provide insights into uplift rates. Interestingly, the rates of reaction during decompression or rapid exhumation can lead to symplectite formation, even if the deformation is not extensive. On the other

hand, a slower uplift combined with significant deformation or fluid inflow could quicken reactions and cause full recrystallization upon decompression. This complex interplay of reactions, which is deduced from the order of isopleths and prograde-retrograde mineral assemblages, illustrates a clockwise metamorphic P-T trajectory for the Sonapahar region.

The P-T path derived from the granulites in this study is characterized by a clockwise trajectory. This path, indicative of initial burial followed by rapid cooling (+ minor decompression), aligns with regional tectonic processes associated with the collision and subsequent exhumation events. Dwivedi *et al.* (2020) also reported a similar clockwise P-T path in their study of granulites from the Sonapahar area, suggesting a coherent tectonothermal evolution across the region. Their findings documented a clockwise P-T path with normal retrograde/decompression for granulites and characterized by peak condition at ~6 kbar – 850°C followed by normal cooling. In contrast, Mahanta *et al.* (2024) (Fig. 6b) demonstrate high-pressure conditions peaking at ~9 kbar and temperatures reaching ~850°C, followed by isothermal decompression for the mafic granulites.

Neo Proterozoic to Early Paleozoic metamorphism affects the Vestfold Hills (Zhao *et al.* 2001), Larsemann Hills (Carson *et al.* 1997) and the Brattstrand Bluffs (Fitzsimons, 1997) in the Prydz Bay area of East Antarctica. The retrograde P-T paths of these areas are relatively similar to the ones found in this study. Probably from the Paleo-Mesoproterozoic, the metapelites residing in the
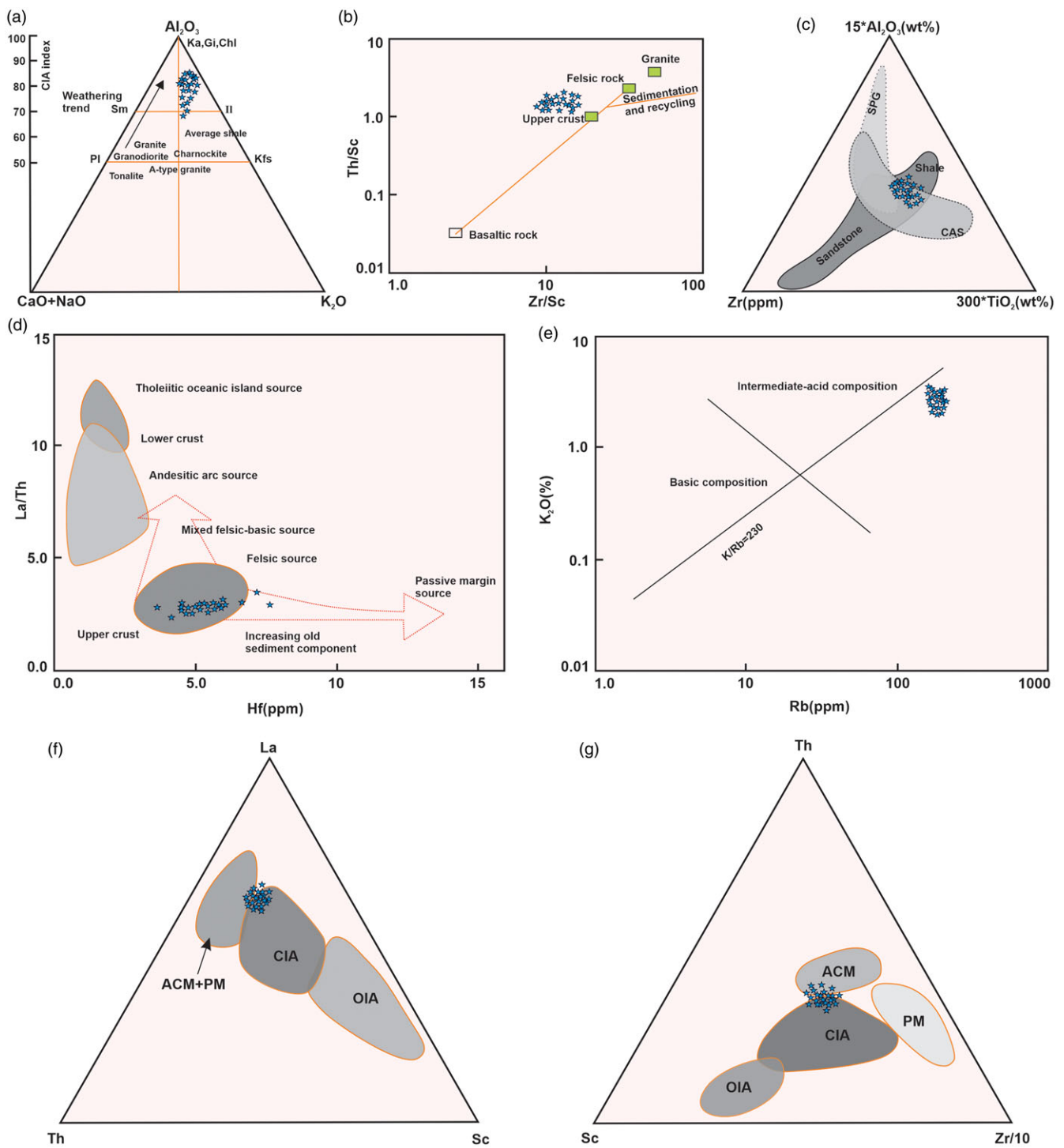
Figure 10. Geochemical diagrams of the samples in the Sonapahar area. (a) Molecular proportions Al$_2$O$_3$-(Na$_2$O + CaO*)-K$_2$O triangular plot (after Fedo *et al.* 1995). Ka, kaolinite; Gi, gibbsite; Chl, chlorite; Sm, smectite; Il, illite; Pl, plagioclase; Kfs, K-feldspar; (b) plot of Th/Sc versus Zr/Sc (McLennan, 1993); (c) Al-Ti-Zr triangular diagram. The solid contour encloses the compositions observed in clastic sediments; CAS represents the field of calc-alkaline suites; SPG represents the field of strongly peraluminous granites (after Garcia *et al.* 1994); (d) La/Th-Hf source rock discrimination diagram (Floyd and Leveridge, 1987); (e) K$_2$O-Rb provenance discrimination diagram (after Floyd and Leveridge, 1987); (f-g) tectonic discrimination diagrams of samples in the Liumao area (after Bhatia and Crook, 1986). Ternary diagrams of La-Th-Sc (f) and Th-Sc-Zr/10 (g). PM = passive margin; ACM = active continental margin; CIA = continental island arc; OIA = oceanic island arc.

mid-crust at the SMGC have been subjected to heating, reaching a peak temperature of above 900°C at roughly 8.4 kb during the Pan-African collision. Similar to the Prydz Bay metapelites, the SMGC metapelites underwent decompression and cooling after reaching peak P-T. As a result, SMGC and the Prydz Bay region had a nearly identical metamorphic history that involved a collisional setting for granulite facies metamorphism during Pan-African orogeny (Chatterjee *et al.* 2011).
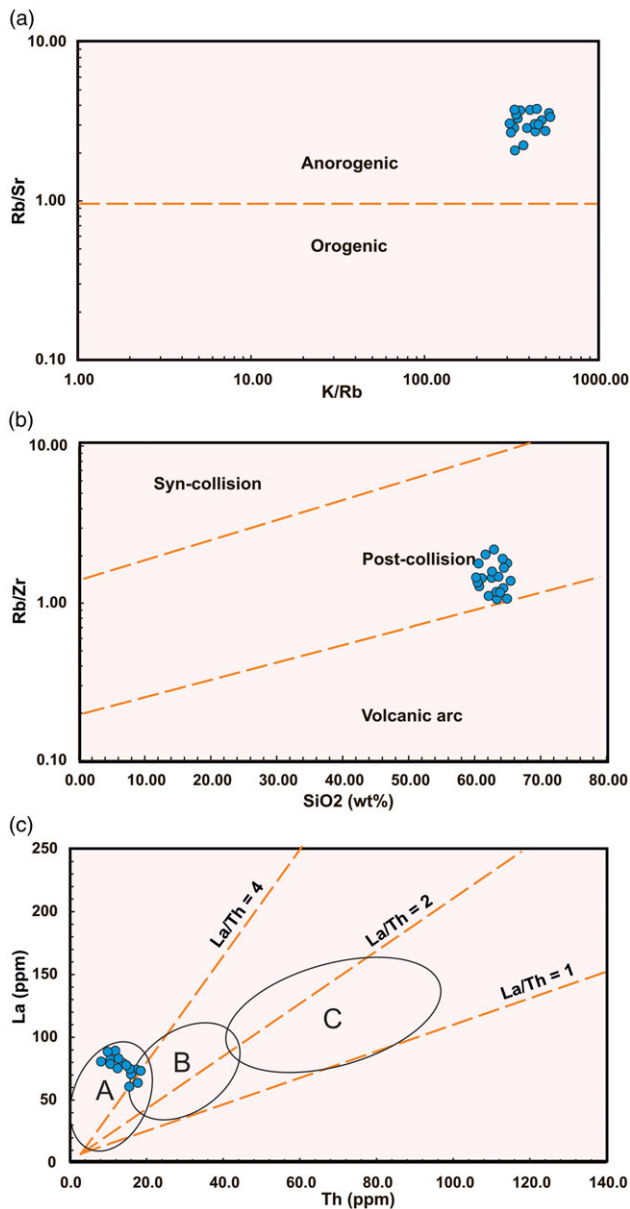
Figure 11. (a) K/Rb vs. Rb/Sr discrimination diagram for orogenic and anorogenic processes; (b) SiO$_2$ vs. Rb/Zr discrimination diagram for syn-collision, post-collision and volcanic arcs; (c) Th vs. La plot showing the dominance of the derived sediments from the passive continental margins and oceanic island arcs.

Table 6. Age calculations with $\Omega = 0.492$. Each age corresponds to a single biotite ablation with the following laser parameters: 50 Hz, 50 pulses by run, 6 runs per analysis (300 pulses in total), 70 μm diameter, 20–25 μm depth, fluence 3.5 J/cm^2

Sample	K (kcps)	^{40}Ar* (moles/g)	Age (Ma)	± 1 s.d.
SN-7F	18.957	10.2289	435	5
SN-7F	19.005	10.4492	432	6
SN-7F	16.108	9.0553	441	6
SN-7F	17.903	10.0801	441	6
SN-7F	19.260	10.8642	442	6
SN-7F	17.317	9.8138	444	6
SN-7F	15.549	8.8732	446	6
SN-7F	17.308	9.8880	447	6
SN-7F	15.181	8.7141	449	6
SN-7F	14.459	8.4610	456	6
		Mean	**442**	**9**
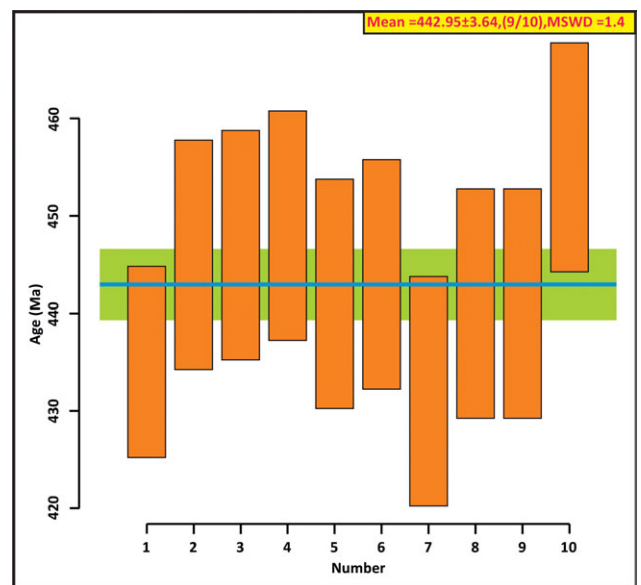
Figure 12. The weighted average of mean ages from biotite in the sample (Sn-7F).

5.c. Geochemical interpretation

The analysis of whole rock data (major and trace) from the Sonapahar region suggests that the protoliths of the examined samples were clay rocks and sandstones. The TiO$_2$-Zr values of the analysed samples indicate a limited range, suggesting poor sorting and rapid sediment deposition. This correlation points to the origin of the studied granulite through intense metamorphism in Proterozoic rocks. Geochemical parameters, including sediment chemistry variations influenced by element mobility during sediment recycling, strongly suggest that the protolith of these pelitic granulites primarily resulted from the partial melting of ancient crustal basement rocks. The contribution of trace elements from upper mantle rocks influenced the geochemical character of the investigated granulitic terrain, indicating the complex interplay of geological events in its formation.

5.d. Geochronology

Taking into account the tectonic implications involved, the combination of K-Ar isotopic age and monazite dates brings attention to the geological history of the Sonapahar Mg-Al granulite. The granulite's journey can be traced from its peak metamorphic stage during the Pan-African thermal event (682.20 ± 28 Ma), as evidenced by monazite chemical dating. Subsequently, it underwent an upward movement towards shallower depths and experienced temperatures around 300°C at 442.95 ± 3.64 Ma. This alignment of the K-Ar age with the temperature at which biotite closes supports a consistent chronological sequence. It is suggested that the presence of an older monazite date (1527 Ma) within the
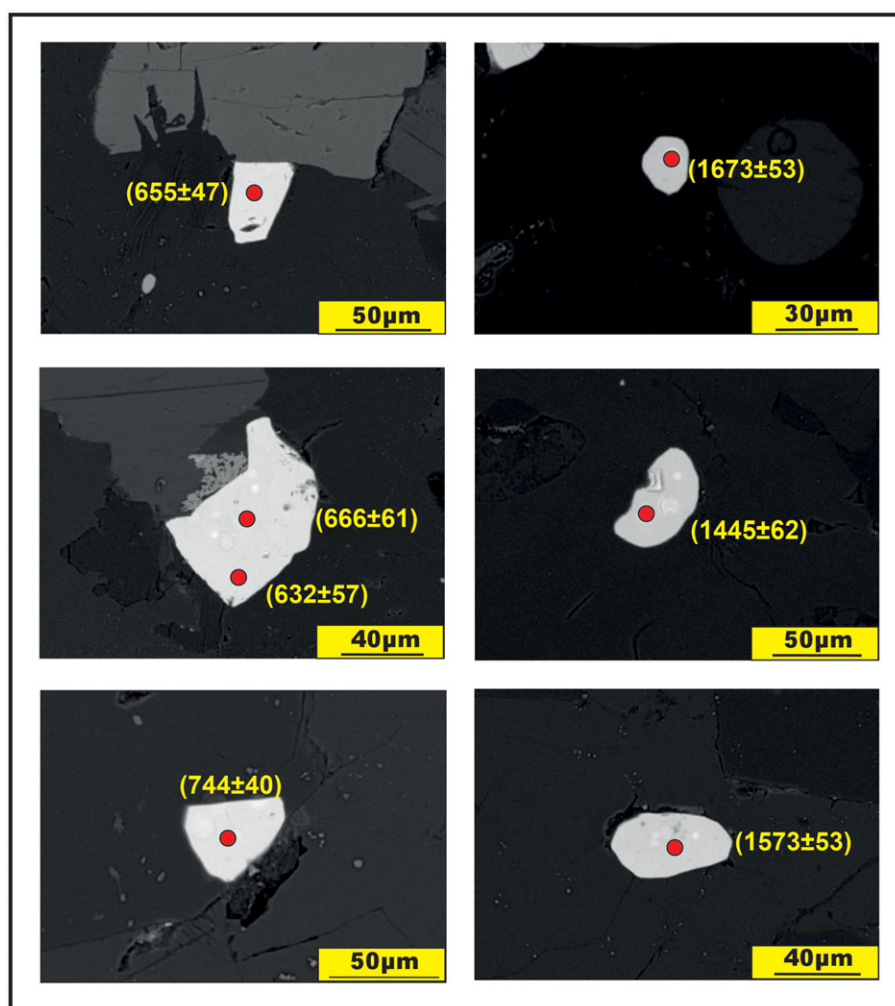
Figure 13. Representative BSE image of monazite grains from sample Sn-7F.

studied sample might be attributed to earlier tectonothermal events, possibly retained within robust minerals like garnet.

The clockwise P-T trajectory obtained through pseudosection modelling, combined with geothermobarometric analysis, geochronology and petrographic observations, gives credibility to the hypothesis that the Sonapahar is the farthest extension of the EGMB. This interpretation is consistent with the model proposed by Crawford (1974).

5.e. Tectonic implications

The monazite found in the study sample (Sn-7F), which occurs as groundmass as well as inclusions within garnet, does not exhibit any visible zoning. The monazite under study has a mean age of 682.20 ± 28 Ma and 1527.4 ± 38 Ma, which corresponds to younger and older (inherited) metamorphic ages, respectively. The majority of the earlier age records in the monazite in the SMGC may have been obliterated by this high-grade event, leaving just the most recent event to be recorded, making it plausible that it is connected to the Pan-African tectonic event that had a global impact. Regardless of their textural predominance in metapelites, monazite grains have historically provided the primary Pan-African age records (Chatterjee *et al.* 2007, 2011). According to Chatterjee *et al.* (2007), the metapelite is of late Cambrian age and was formed by the thermal reworking of monazite in the later phase of Pan-African orogeny, which is also reported by Mahanta

et al. (2024) from mafic rocks of Sonapahar and correlate it with the Kuunga orogeny. Comparisons of the geochronological ages noted by various researchers from various portions of the SMGC, including the monazite ages documented in this work, show that the SMGC as a whole has been impacted by many stages of deformation and its associated metamorphism.

The Pan-African event, which occurred approximately 700–500 million years ago during the Proterozoic–earliest Paleozoic era, was one of the largest orogenies in Earth's history (Mallard & Rogers, 1997). The Pan-African Orogeny refers to the geological process that occurred between 600 and 500 Ma, 650 and 550 Ma or perhaps 950 and 500 Ma, during which the Gondwana supercontinent was formed. This process involved significant tectonic and thermal activity in the Earth's crust (Kröner and Stern, 2004; Stern, 1994). Gondwana accretion occurred over a long period, approximately 850 to 520 million years ago (e.g., Grunow *et al.* 1996; Dalziel, 1991). Significant accretion occurred primarily between 650 and 520 million years ago (Collins and Pisarevsky, 2005; Meert, 2003). Due to its extensive distribution and prolonged duration, the Pan-African event was not regarded as a singular orogeny. The process is, in fact, a lengthy orogenic cycle that entails the repeated opening and closing of enormous ocean basins, as well as the accretion and collisions of drifting continental blocks.

In this study, we have obtained a Pan-African age of 682.20 ± 28 Ma from the studied granulite. This suggests that the Pan-African event started its influence over SMGC during the

Table 7. EPMA dating age of monazite crystal of the studied rock (Sn-7F)

| Oxides	1	2	3	4	5	6	7	8	9	10	11	12	13	14	15	16	17	18	19	20	21	22	23	24
Al_2O_3	0.00	0.00	0.00	0.00	0.04	0.00	0.00	0.03	0.19	0.02	0.00	0.00	0.01	0.00	0.05	0.00	0.00	0.00	0.00	0.00	0.00	0.00	0.05	0.09
SiO_2	0.00	0.26	0.31	0.22	0.29	0.20	0.20	0.81	0.88	0.67	0.29	0.34	0.24	0.46	0.35	0.42	0.36	0.43	0.47	0.48	0.50	0.46	0.59	0.41
P_2O_5	30.04	29.04	28.88	29.41	29.27	29.27	29.03	28.42	29.07	27.96	29.17	28.99	28.70	28.72	29.15	28.86	29.21	29.03	29.11	29.07	29.21	29.18	29.03	29.34
CaO	1.26	1.37	1.23	1.14	1.22	1.13	1.37	1.04	0.90	1.02	1.17	1.14	1.38	0.87	0.75	1.15	0.63	0.92	0.94	1.14	0.99	0.86	0.91	1.11
La_2O_3	12.90	12.40	12.20	12.52	12.91	12.33	12.87	10.81	12.67	10.52	13.58	13.56	12.98	12.34	12.61	11.85	12.71	12.03	12.12	12.27	12.21	12.09	12.41	12.67
Ce2O3	26.34	25.42	26.25	25.97	26.83	27.19	27.36	26.36	25.98	24.72	27.29	27.22	26.92	26.62	27.39	25.79	26.92	26.04	26.48	26.15	25.85	26.77	26.85	27.13
Pr_2O_3	3.87	2.91	2.84	2.95	2.95	3.14	3.36	3.61	2.95	3.20	3.30	3.13	2.98	3.31	3.35	3.22	3.42	3.10	3.48	3.05	3.04	3.00	3.12	2.94
Nd_2O_3	11.57	10.81	11.36	11.35	11.12	11.50	11.37	12.49	10.59	11.89	11.36	11.64	11.51	11.17	11.18	10.77	11.44	11.52	11.46	10.85	11.33	11.07	11.61	11.47
Sm_2O_3	2.77	1.78	1.60	1.76	1.93	1.93	1.71	1.98	1.73	2.10	1.76	1.75	1.78	1.82	2.09	1.76	1.73	1.90	1.59	1.74	2.05	1.84	1.90	1.90
Eu_2O_3	1.33	0.20	0.19	0.11	0.19	0.13	0.36	0.14	0.04	0.05	0.15	0.07	0.37	0.01	0.09	0.00	0.00	0.00	0.00	0.00	0.05	0.00	0.02	0.05
Gd_2O_3	2.99	1.63	1.46	1.48	1.54	1.39	1.30	1.85	1.61	2.10	1.44	1.99	1.20	1.66	1.73	1.75	1.94	1.96	1.90	1.87	1.70	1.74	1.88	1.86
PbO	0.17	0.14	0.19	0.17	0.14	0.15	0.18	0.19	0.19	0.19	0.28	0.25	0.41	0.39	0.26	0.40	0.42	0.40	0.34	0.55	0.47	0.37	0.32	0.29
ThO_2	4.58	4.66	5.95	4.35	4.64	4.74	5.00	6.45	5.33	6.35	6.66	5.66	5.60	5.05	3.41	5.36	5.25	4.96	4.05	6.96	5.59	4.83	3.87	3.52
UO_2	0.28	0.11	0.23	0.27	0.13	0.20	0.22	0.12	0.19	0.13	0.64	1.11	0.29	0.24	0.20	0.28	0.27	0.17	0.19	0.30	0.35	0.19	0.21	0.17
Y_2O_3	2.48	2.71	2.27	2.61	2.55	2.80	1.52	2.45	2.51	3.35	1.01	2.69	2.05	3.07	3.10	3.04	2.89	3.18	3.13	3.31	3.00	3.15	3.13	3.18
Total	100.59	93.45	94.95	94.32	95.76	96.11	95.85	96.75	94.84	94.25	98.09	99.53	96.42	95.74	95.70	94.66	97.20	95.64	95.27	97.74	96.33	95.56	95.89	96.11
Age (Ma)	730	668	655	734	666	632	718	645	758	664	744	623	1439	1502	1428	1445	1530	1637	1621	1573	1555	1528	1571	1593
Age error(±2 s.d.)	57	62	47	59	61	57	54	46	53	47	40	36	52	67	92	62	65	73	84	53	60	73	86	95
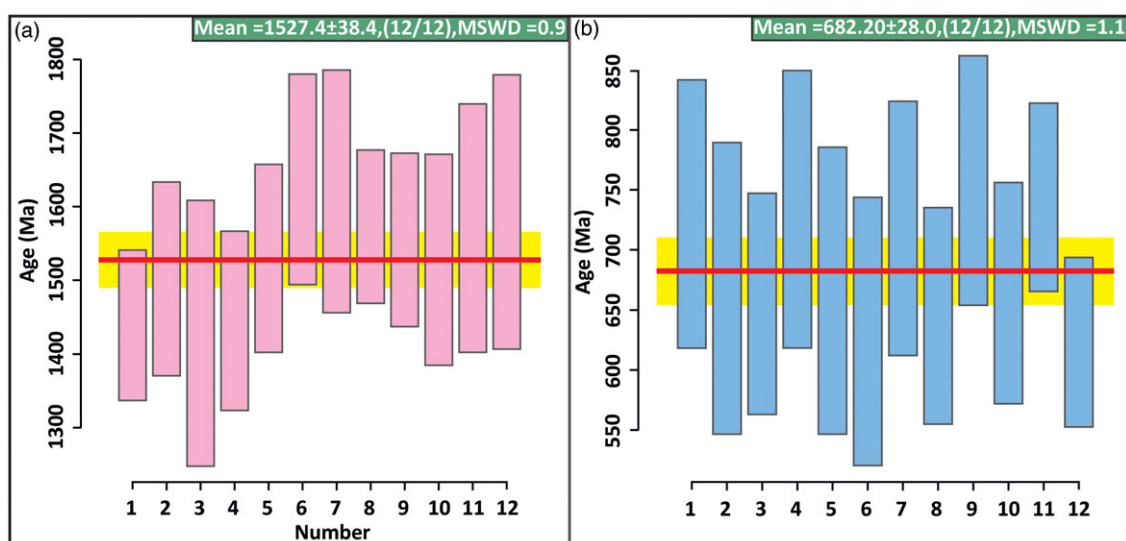
Figure 14. (a) Representative graphs of weighted average of the distributions showing a mean age of 1527 Ma for the old thermal event; (b) representative graphs of weighted average of the distributions showing a mean age of 682 Ma for the thermal reworking event; (c) representative graph, combinedly showing the probability density plot of two thermal events.
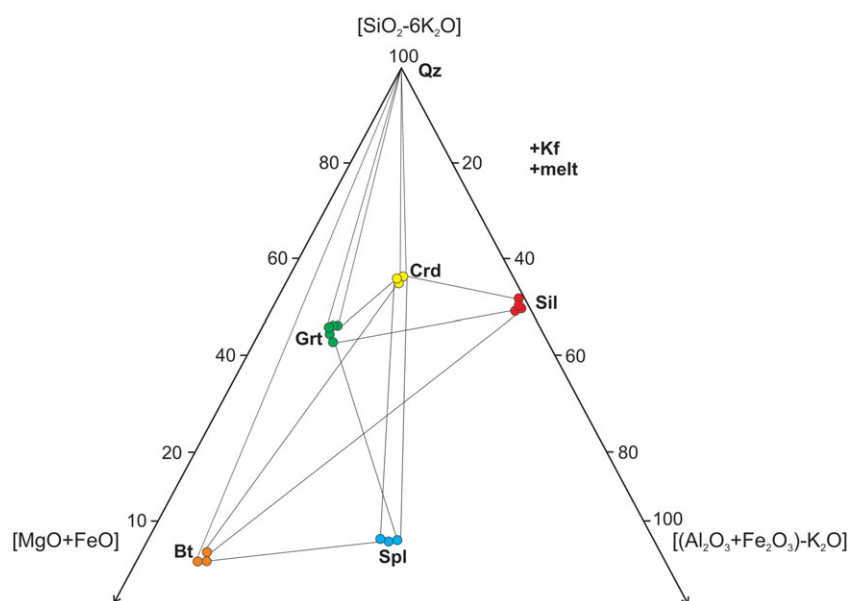

Figure 15. Phase relations shown in the (SiO_2-6K_2O)-(Fe-Mg)O-(Al, Fe^{3+}, Cr_2O_3-K_2O) for Spinel + quartz bearing granulites (modified after Prakash *et al.* 2020).

Cryogenian Period. Whereas earlier literature from the study area reported a much younger age of around (ca. 570–480 Ma) from the same domain (Chatterjee *et al.* 2007, Mahanta *et al.* 2024). Mahanta *et al.* (2024) further correlate this age with the final phase of Pan-African orogeny, i.e. Kuunga Orogeny, suggesting the possibility of the Pan-African resetting effect. This could probably be due to a pair (or more) tectono-metamorphic events that have influenced SMGC during Pan-african orogeny, which is similar to the Pan-African event reported in the EA and EAO (Liudong *et al.* 2018).

Moreover, during the East Gondwana assembly, the Prydz orogenic belt along the Prydz Bay to Denman Glacier along with EGMB and SMGC may represent the collision zone of this orogeny (Liudong *et al.* 2018). Chatterjee *et al.* (2007) highlighted the western boundary of the Pan-African collision zone involving India, Australia and Antarctica. The SMGC was most likely the leading edge of an oblique collision between India and Australo-Antarctica in the Rodinia supercontinent's reconstructed Neoproterozoic-Cambrian assembly. The SMGC exhibits several similarities with its counterparts in the Prydz Bay region of East Antarctica (Chatterjee *et al.*, 2007), owing to the predominant of Pan-African dates and the presence of late tectonic Cambro-Ordovician-Neoproterozoic granites in the reconstructed collision setting (Fig. 16). The Pan-African suture, which crossed via Prydz Bay in Antarctica and entered India via the SMGC, might have continued north via the Sonapahar and Garo-Goalpara Hills regions.

The older monazite grain (1527 Ma) found in this study, however, may be connected to the high-grade metamorphism link between the pre-Grenvillian and Palaeoproterozoic eras. In the SMGC, widespread granite magmatism occurred between 1800 and 1400 Ma as a result of pre-Grenvillian tecnonothermal
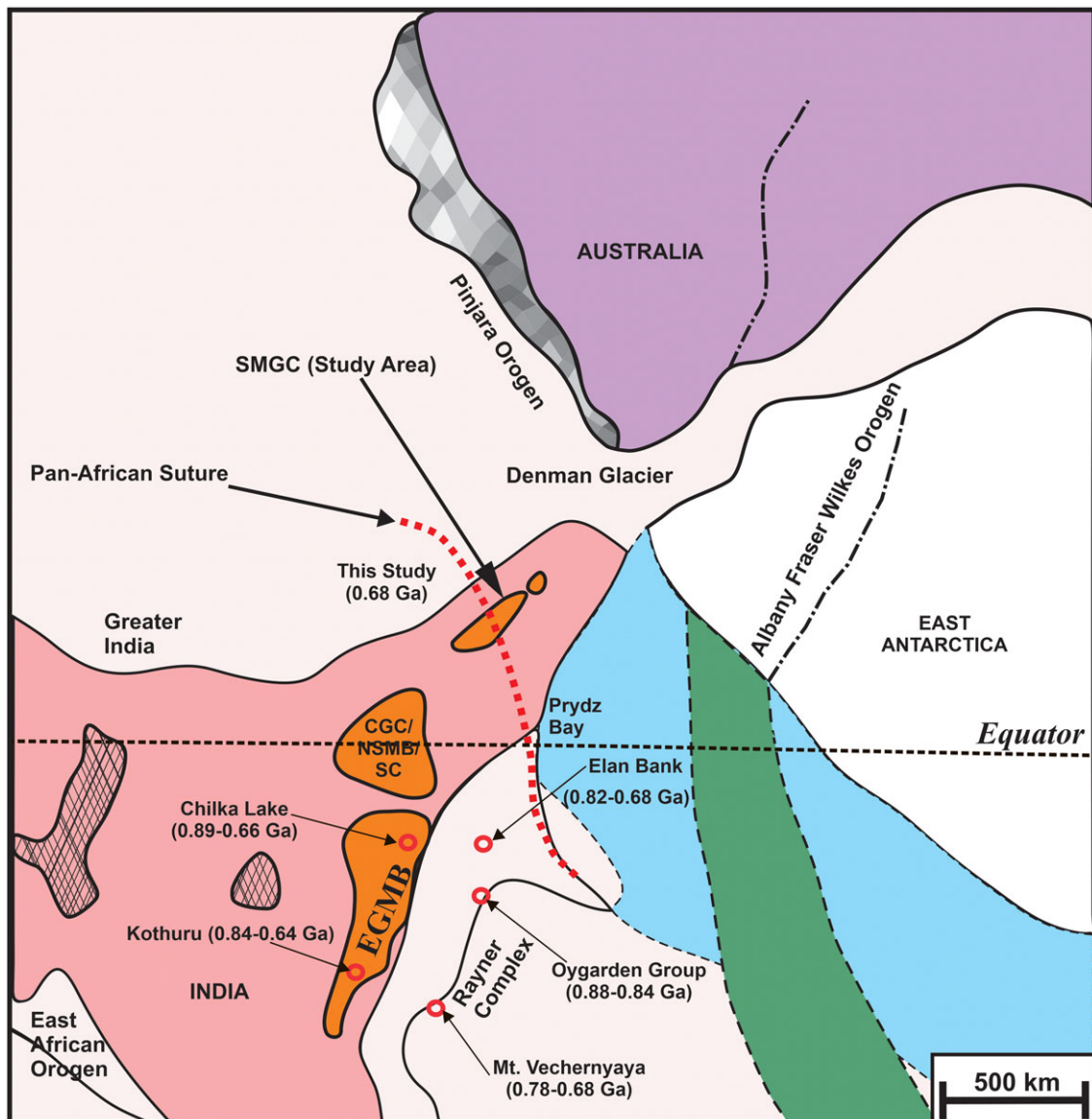
Figure 16. Reconstruction of the early Neoproterozoic supercontinent showing the correlation between Greater Indian Landmass and Eastern Antarctica. SMGC – Shillong Meghalaya Gneissic Complex, CGC – Chotanagpur Gneissic Complex, NSMB – Northern Singhbhum Mobile Belt, SC – Singhbhum Craton, and EGMB – Eastern Ghats Mobile Belt. A Possible extent of the Pan-African suture through Prydz Bay and the SMGC is shown by the Dotted line (modified after Chatterjee *et al.* 2007).

processes, which correlate to the Columbia supercontinent (Kumar *et al.* 2017a; Yin *et al.* 2010). Notably, the older dates are quite uncommon in the Mg-Al granulites, which most likely indicates that these monazites were crystallized during or after the first cycle of deformation-metamorphism's cooling phase. The age corresponds to ~1.5 Ga, which may have been connected to a later stage of the Columbia supercontinent's assembly, which is thought to have begun at ~1.8 Ga (Li *et al.* 2008; Rogers and Santosh, 2002; Zhao *et al.* 2004). Coastal East Antarctica is connected to India (Greater India) in all widely recognized reconstructions (Li *et al.* 2008; Rogers and Santosh, 2002; Zhou *et al.* 2002), while the remainder of East Antarctica (Mawson Craton) is connected to South Australia. Thus, it is unclear, therefore, how India and coastal East Antarctica came to be connected. The Rayner–Napier Complexes have events of around 1.6 Ga in age (Kelley, 2002; Owada *et al.* 2003), although it is unclear how these events relate to collisions or the formation of the Columbia supercontinent.

6. Conclusion

The present study delivers a multi-faceted understanding of the geological and tectonic complexities underlying the Sonapahar region. The study sheds light on the rock classifications, metamorphic processes, geochemical signatures and temporal markers that collectively contribute to a more comprehensive comprehension of the geological history of the region and its broader implications in the context of plate tectonics and continental amalgamation.

The primary findings encompass several key aspects:

1. P-T Evolutionary Path: Findings reveal a clockwise pressure-temperature (P-T) evolutionary path. This suggests an initial phase of decompression, followed by subsequent cooling processes.
2. Metamorphic Conditions: By using a variety of techniques, including traditional thermobarometry, pseudosection

modeling, and the winTWQ software, the observed P-T conditions indicate high to UHT metamorphism.

3. Geochemical Rock Analysis: Major and trace element data imply that clay rocks and sandstones with a predominately felsic provenance that originated in a continental island arc environment may have been the protoliths of the metamorphic rocks in the Sonapahar area.

4. Monazite Dating and Tectonic Events: The monazite chemical dating shows the prevalence of Neo-Proterozoic metamorphic age (dated at approximately 682 million years ago) within the central region of the Sonapahar area (SMGC). This age could potentially be linked to the broader context of the Pan-African collision event between the landmasses of India and Australia-Antarctica. This collision, an essential episode during the assembly of East Gondwana, holds global significance. The preponderance of earlier monazite grain (1527 Ma) identified in this study could be linked to the final phase of the Columbia supercontinent's formation.

References

Abdel-Rahman AM and El-Kibbi MM (2001) Anorogenic magmatism. chemical evolution of the Mount El-Sibai A-type complex Egypt, and implications for the origin of within-plate felsic magmas. *Geological Magazine* **138**, 67–85.

Aranovich LY and Podlesskii KK (1983) The Cordierite-Garnet-Sillimanite-Quartz equilibrium: experiments and applications. In *Kinetics and Equilibrium in Mineral Reactions.* Advances in Physical Geochemistry (ed SK Saxena), vol 3. doi: 10.1007/978-1-4612-5587-1_6

Aranovich LY and Podlesskii KK (1989) Geothermobarometry of high-grade metapelites: simultaneously operating reactions. *Geological Society, London, Special Publications* **43**, 45–61. doi: 10.1144/GSL.SP.1989.043.01.03

Asiedu DK, Suzuki S, Nogami K and Shibata T (2000) Geochemistry of Lower Cretaceous sediments Inner Zone of South-west Japan. constraints on provenance and tectonic environment. *Geochemistry Journal* **34**, 155–73.

Bhattacharya A, Mohanty L, Maji A, Sen SK and Raith M (1992) Non-ideal mixing in the phlogopite-annite binary: constraints from experimental data on Mg-Fe partitioning and a reformulation of the biotite-garnet geothermometer. *Contribution to Minerology and Petrology* **111**, 87–93.

Benisek A, Dachs E and Kroll H (2010) A ternary feldspar-mixing model based on calorimetric data, p. development and application. *Contributions to Mineralogy and Petrology* **160**, 327–37, p. https://doi.org/10.1007/s00410-009-0480-8

Berman RG (2006) winTWQ version 2.3), p. A Software Package for Performing Internally-Consistent Thermobarometric Calculations, p. Geological Survey of Canada, Open File 5462, p. 41.

Berman RG and Aranovich LY (1996) Optimized standard state and solution properties of minerals, p. *Contributions to Mineralogy and Petrology* **126**, 1–24.

Bhat MI and Ghosh SK (2001) Geochemistry of the 2.51 Ga old Rampur group pelites western Himalayas. implications for their provenance and weathering. *Precambrian Research* **108**, 1–16.

Bhatia MR (1983) Plate tectonics and geochemical composition of sandstones. *Journal of Geology* **91**, 611–27.

Bhatia MR (1984) Composition and classification of Paleozoic flysch mudrocks of eastern Australia. Implications in provenance and tectonic setting interpretation. *Sedimentary Geology* **41**, 249–68.

Bhatia MR (1985) Rare earth element geochemistry of Australian Paleozoic graywackes and mudrocks: Provenance and tectonic control. *Sedimentary Geology* **45**, 97–113.

Bhatia MR and Crook KAW (1986) Trace element characteristics of graywackes and tectonic setting discrimination of sedimentary basins. *Contributions to Mineralogy and Petrology* **92**, 181–93.

Bhowmik SK, Wilde SA, Bhandari, A. and Basu SA (2014) Zoned monazite and zircon as monitors for the thermal history of granulite terranes. an example from the Central Indian Tectonic Zone. *Journal of Petrology* **55**, 585–621.

Bidyananda M and Deomurari MP (2007) Geochronological constraints on the evolution of Meghalaya massif, northeastern India, p. an ion microprobe study, p. *Current Science* **93**, 1620–23.

Carson CJ and Hand M (1997) P.H.G.M. Dirks stable coexistence of grandidierite and kornerupine during medium pressure granulite facies metamorphism. *Mineralogical Magazine* **59**, 327–39.

Chatterjee N, Bhattacharya A, Duarah BP and Mazumdar AC (2011) Late Cambrian reworking of Palaeo-Mesoproterozoic granulites in Shillong–Meghalaya Gneissic Complex Northeast India, p. Evidence from PT pseudosection analysis and monazite chronology and implications for East Gondwana assembly, p. *Journal of Geology* **119**, 311–30.

Chatterjee N, Mazumdar AK, Bhattacharya A and Saikia RR (2007) Mesoproterozoic granulites of the Shillong– Meghalaya Plateau, p. evidence of westward continuation of the Prydz Bay Pan-African suture into northeastern India, p. *Precambrian Research* **152**. 1–26.

Collins AS and Pisarevsky SA (2005) Amalgamating eastern Gondwana: The evolution of the Circum-Indian orogens. *Earth-Science Reviews* **71**, 229–70. doi: 10.1016/j.earscirev.2005.02.004

Connolly JAD (2005) Computation of phase equilibria by linear programming, p. a tool for geodynamic modeling and its application to subduction zone decarbonation. *Earth and Planetary Science Letters* **236**(1-2), 524–41.

Connolly JAD (2009) The geodynamic equation of state, p. what and how. *Geochemistry, Geophysics, Geosystems* **10**(10). doi: 10.1029/2009GC002540

Cox R, Lowe DR and Cullers RL (1995) The influence of sediment recycling and basement composition on evolution of mudrock chemistry in the southwestern United States. *Geochimica et Cosmochimica Acta* **59**, 2919–40.

Crawford AR (1974) Indo-Antarctica, Gondwana Land and pattern of the distortion of a granulite belt, p. *Tectonophysics* **22**, 141–57.

Dalziel IW (1991) Pacific margins of Laurentia and East Antarctica–Australia as a conjugate rift pair: evidence and implications for an Eocambrian supercontinent. *Geology* **19**, 598–601.

Desikachar SV (1974) A review of the tectonic and geological history of eastern India in terms of plate tectonics theory, p. *Journal of Geological Society of India* **15**, 137–49.

Dwivedi SB, Theunuo K and Kumar RR (2020) Characterization and metamorphic evolution of Mesoproterozoic granulites from Sonapahar

Meghalaya), NE India, using EPMA monazite dating. *Geological Magazine* **157**(9), 1409–27.

Evans P (1964) The tectonic framework of Assam, p. *Journal of Geological Society of India* **5**, 80–96.

Fedo CM, Nesbitt HW and Young GM (1995) Unraveling the effects of potassium metasomatism in sedimentary rocks and paleosols with implications for paleowearhering conditions and provenance. *Geology* **23**, 921–24.

Ferry JT and Spear FS (1978) Experimental calibration of the partitioning of Fe and Mg between biotite and garnet, p. *Contributions to Mineralogy and Petrology* **66**, 113–17.

Fitzsimons ICW (1997) The Brattstrand paragneiss and the Sostrene orthogneiss: a review of Pan-African metamorphism and Grenvillian relics in southern Prydz Bay. In *The Antarctic Region: Geological Evolution and Processes* (ed Ricci CA), pp. 121–130. Siena: Terra Antarctic Publications.

Floyd PA and Leveridge BE (1987) Tectonic environment of the Devonian Gramscatho basin south Cornwall. framework mode and geochemical evidence from turbiditic sandstone. *Journal of the Geological Society of London* **144**, 531–42.

Ganguly J and Saxena SK (1984) Mixing properties of aluminosilicates garnets: constraints from natural and experimental data, and applications to geo-thermo-barometry. *American Mineralogist* **69**, 88–97.

Garcia D, Fonteilles M and Moutte J (1994) Sedimentary fractionations between Al Ti and Zr and the genesis of strongly peraluminous granites. *The Journal of Geology* **102**, 411–22.

Ghosh S, Bhalla JK, Paul DK, Sarkar A, Bishui PK and Gupta SN (1991) Geochronology and geochemistry of granite plutons from East Khasi Hills, Meghalaya, p. *Journal of the Geological Society of India* **37**, 331–42.

Ghosh S, Chakraborty S, Paul DK, Bhalla JK, Bishui PK and Gupta SN (1994) New Rb–Sr isotopic ages and geochemistry of granitoids from Meghalaya and their significance in middle to late Proterozoic crustal evolution, p. *Indian Minerals* **48**, 33–44.

Ghosh S, Fallick AE, Paul DK and Potts PJ (2005) Geochemistry and origin of Neoproterozoic granitoids of Meghalaya, Northeast India, p. implications for linkage with amalgamation of Gondwana Supercontinent, p. *Gondwana Research* **8**, 421–32.

Gromet LP, Dymek RF, Haskin LA and Korotev RL (1984) The North American Shale Composite. its composition major and trace element characteristics. *Geochimica et Cosmochimica Acta* **48**, 2469–82.

Grunow A, Hanson R and Wilson T (1996) Were aspects of Pan-African deformation linked to Iapetus opening? *Geology* **24**, 1063–6.

Harley SL (2020) UHT Metamorphism. Reference Module in Earth Systems and Environmental Sciences. DOI: 10.1016/B978-0-12-409548-9.12543-6.

Harris NBW, Pearce JA and Tindle AG (1986) Geochemical characteristics of collision-zone magmatism. *Journal of the Geological Society of London Special Publications* **19**, 67–81.

Herron MM (1988) Geochemical classification of terrigenous sands and shales from core or log data. *Journal Sedimentary Petrology* **58**, 820–29.

Hodges KV and Spear FS (1982) Geothermometry, geobarometry and the Al_2SiO_5 triple point at Mt. Moosilauke, New Hampshire, p. *American Mineralogist* **67**, p. 1118–34.

Holland TJB and Powell R (1998) An internally consistent thermodynamic data set for phases of petrological interest, p. *Journal of Metamorphic Geology* **16**(3), 309–43.

Holland TJB and Powell R (2011) An improved and extended internally consistent thermodynamic dataset for phases of petrological interest, involving a new equation of state for solids. *Journal of Metamorphic Geology* **29**, 333–83.

Hörmann PK, Raith M, Raase P, Ackermand D and Seifert F (1980) The granulite complex of Finnish Lapland, p. petrology and metamorphic condition in the Ivalojokii-Inarijarvi, area, p. *Bulletin of the Geological Survey of Finland* **308**, 1–95.

Kelley S (2002) K-Ar and Ar-Ar dating, p. *Reviews in Mineralogy and Geochemistry* **47**, 785–818.

Kelsey D and Hand M (2015) On ultrahigh temperature crustal metamorphism: Phase equilibria, trace element thermometry, bulk composition, heat sources, timescales and tectonic settings. *Geoscience Frontiers* **6**(3), 311–56. doi: 10.1016/j.gsf.2014.09.006

Kröner A and Stern RJ (2004) Pan-African orogeny. *In Encyclopedia of Geology* (Selley RC, Cocks LRM, Plimer IR, eds), vol. 1, pp. 1–11.

Kumar S, Rino V, Hayasaka Y, Kimura K, Raju S, Terada K and Pathak M (2017a) Contribution of Columbia and Gondwana supercontinent assembly and growth-related magmatism in the evolution of the Meghalaya Plateau and the Mikir Hills, Northeast India, p. Constraints from U–Pb SHRIMP zircon geochronology and geochemistry, p. *Lithos* **277**, 356–77.

Kumar S, Pieru T, Rino V and Hayasaka V (2017b) Geochemistry and U–Pb SHRIMP zircon geochronology of microgranular enclaves and host granitoids from the South Khasi Hills of the Meghalaya Plateau, NE India, p. evidence of synchronous mafic–felsic magma mixing–fractionation and diffusion in a post-collision tectonic environment during the Pan-African orogenic cycle. *Geological Society, London, Special Publications* **457**, 253–89. doi: 10.1144/ SP457.10

Lal ML, Ackermand D, Seifert F and Halder SK (1978) Chemographic relationship in sapphirine bearing rocks from Sonapahar, Assam, India, p. *Contributions to Mineralogy and Petrology* **67**(2), 169–87.

LaMaskin TA, Dorsey RJ and Vervoort JD (2008) Tectonic controls on mudrock geochemisry Mesozoic rocks of Eastern Oregon and Western Idaho U.S.A. Implications for Cordilleran tectonics. *Journal of Sedimentary Research* **78**, 765–83.

Li QG, Liu SW, Han BF, Zhang J and Chu ZY (2005) Geochemistry of metasedimentary rocks of the Proterozoic Xingxingxia Complex. Implications for provenance and tectonic setting of the Eastern segment of the central Tianshan Tectonic zone Northwestern China. can. *Journal of Earth Science* **42**, 287–306.

Li ZX, Bogdanova SV, Davidson A, Collins AS, De Waele B, Ernst RE, Fitzsimons ICW, Fuck RA, Gladkochub DP, Jacobs J, Karlstrom KE, Lu S, Natapov LM, Pease V, Pisarevsky SA, Thrane K and Vernikovsky V (2008) Assembly, configuration, and break-up history of Rodinia: a synthesis. *Precambrian Research* **160**, 179–210.

Liudong R, Shi Z, Yanbin W and Chong L (2018) Distribution domains of the Pan-African event in East Antarctica and adjacent areas. *Advances in Polar Science* **29**, 87–107.

Lonker SW (1981) The P-T-x relations of the cordieritegarnet-sillimanite-quartz equilibria, p. *American Journal of Science* **281**, 1056–90.

Mahanta B, Prakash D, Kumar M, *et al.* (2024) Geochemistry, Monazite (U–Pb–Th) Geochronology, and P-T Pseudosection modelling of two-pyroxene mafic granulite from Sonapahar, Shillong Meghalaya gneissic complex, India: Implication for tectono-metamorphic evolution and Global Pan-African correlation. *Geochemistry International* **62**, 574–608. https://doi.org/10.1134/S0016702924700319

Mallard LD and Rogers JJW (1997) Relationship of Avalonian and Cadomian terranes to Grenville and Pan-African events. *Journal of Geodynamics* **23**, 197–221.

McLennan SC, Nance WB and Taylor SR (1980) Rare earth element thorium correlations in sedimentary rocks and the composition of the continental crust. *Geochimica et Cosmochimica Acta* **44**, 1833–39.

McLennan SM (1993) Weathering and global denudation. *The Journal of Geology* **101**, 295–303.

Meert JG (2003) A synopsis of events related to the assembly of eastern Gondwana. *Tectonophysics* **362**, 1–40.

Mitra SK (1998) Structural history of the rocks of the Shillong Group around Sohiong, east Khasi hills, Meghalaya, p. *Indian Journal of Geology* **70**, 123–31.

Nandy, D.R. (1980) Tectonic patterns in northeastern India, p. *Indian Journal of Earth Sciences* **7**, 103–07.

Nandy DR (2001) Geodynamics of North Eastern India and the adjoining region, p. Calcutta, p. ACB Publication, 120.

Neogi S and Pal T (2021) Metasomatically controlled sillimanite–corundum deposit, p. A case study from Sonapahar, Meghalaya, Northeast India, p. *Journal of Earth System Science* **130**(3), 120.

Nesbitt HW and Young GM (1982) Early Proterozoic climates and plate motions inferred from major element chemistry of lutites. *Nature* **299**, 715–17.

Nesbitt HW and Young GM (1984) Prediction of some weathering trends of plutonic and volcanic rocks based on thermodynamic and kinetic considerations. *Geochimica et Cosmochimica Acta* **48**, 1523–34.

Nesbitt HW and Young GM (1989) Formation and diagenesis of weathering profiles. *The Journal of Geology* **97**, 129–47.

Nichols GT, Berry RF and Green DH (1992) Internally consistent gahnitic spinel-cordierite-garnet equilibria in the FMASHZn system: geothermobarometry and applications. *Contributions to Mineralogy and Petrology* **111**, 362–77. doi: 10.1007/BF00311197

Owada M, Baba S, Läufer A, Elvebold S, Shiraishi K and Jacobs J (2003) Geology of eastern Mühlig-Hofmannfjella and Filchnerfjella in Dronning Maud Land, East Antarctica: a preliminary report on a JapanNorway-Germany joint geological investigation. *Polar Geoscience* **16**, 108–36.

Panahi A, Young GM and Rainbird RH (2000) Behavior of major and trace elements including REE, during Paleoproterozoic pedogenesis and diagenetic alteration of an Archean granite near Ville Marie Quebec Canada. *Geochimica et Cosmochimica Acta* **64**, 2199–220.

Pandey M, Pandit D, Arora D, Rao NC and Pant NC (2019) Analytical protocol for U-Th-Pb chemical dating of monazite using CAMECA SXFive EPMA installed at the mantle petrology laboratory, Department of Geology, Banaras Hindu University, Varanasi, India. *Journal of the Geological Society of India* **93**, 46–50.

Perchuk LL (1991) Derivation of a thermodynamically consistent set of geothermometers and geobarometers for metamorphic and magmatic rocks, In *Progress in metamorphic and magmatic petrology*, 93–112. Cambridge University Press, p. https://doi.org/10.1017/CBO9780511564444.

Pigage LC and Greenwood, HJ (1982) Internally consistent estimates of pressure and temperature; the staurolite problem, p. *American Journal of Science* **282**(7), 943–69.

Prakash D, Patel DK, Yadav MK, Vishal V, Tewari S, Yadav R, Rai SK and Singh CK (2020) Prograde polyphase regional metamorphism of pelitic rocks, NW of Jamshedpur, eastern India: constraints from textural relationship, pseudosection moderlling and geothermobarometry. *Geological Magazine* **157**, 1045–67.

Rogers JJW and Santosh M (2002) Configuration of Columbia, a Mesoproterozoic supercontinent. *Gondwana Research* **5**, 5–22.

Roser BP and Korsch RJ (1986) Determination of tectonic setting of sandstone-mudstone suites using SiO2 content and K2O /Na2O ratio. *Journal of Geology* **94**, 635–50.

Roser BP and Korsch RJ (1988) Provenance signatures of sandstone-mudstone suites determined using discriminant function analysis of major-element data. *Chemical Geology* **67**, 119–39.

Sengupta PR and Agarwal NK (1998) The tectonic segments of Northeastern India and associated gold mineralization, p. *Journal of Geological Society of India* **52**(5), 549–56.

Simonen A (1953) Stratigraphy and sedimentation of the Svecofennidie Early Archean supracrustal rocks in southwestern Finland. *Bulletin of the Geological Society of Finland* **160**, 1–64.

Spear FS and Pyle JM (2010) Theoretical modeling of monazite growth in a low-Ca metapelite. *Chemical Geology* **273**, 111–9.

Stern RJ (1994) Arc assembly and continental collision in the Neoproterozoic East African Orogen: implications for the consolidation of Gondwanaland. *Annual Reviews Earth Planetary Sciences* **22**, 319–51.

Taylor SR and McLennan SM (1985) *The Continental Crust. Its Composition and Evolution*. Oxford, UK: Blackwell. 1–312.

Taylor SR and McLennan SM (1995) The geochemical evolution of the continental crust. *Reviews of Geophysics* **33**, 241–65.

Thompson AB (1976) Mineral reactions in pelitic rocks, p. I. Prediction of P-T-X Mg-Fe), Phase relations, p. *American Journal of Science* **276**, 401–24.

Van de Kamp PC and Leake BE (1985) Petrography and geochemistry of feldspathic and mafic sediments of the northeastern Pacific margin. *Transactions of the Royal Society of Edinburgh: Earth Sciences*, **76**, 411–99.

Vernon RH and Clarke GL (2008) *Principles of Metamorphic Petrology.* Cambridge University Press.

Vielzeuf D (1983) The spinel and quartz associations in high grade xenoliths from Tallante SE Spain, and their potential use in geothermometry and barometry, p. *Contributions to Mineralogy and Petrology* **82**, 301–11.

Wang RM, He GP, Chen ZZ, Zheng SY and Geng YS (1987) Graphical Discriminance of the Protolith of Metamorphic Rocks. Beijing. Geological Publishing House in Chinese,

Weaver CE (1989) *Clays muds and shales.* Amsterdam The Netherlands: Elsevier. 1–820.

Wei ZY, Yu JH, Wang LJ and Shu LS (2009) Geochemical features and tectonic significances of Neoproterozoic metasedimentary rocks from Nanling Range. Geochimica, 38, 1–19.

Wells PRA (1979) Chemical and thermal evolution of archaen sialic Crust, Southern West Greenland. *Journal of Petrology* **20**, 187–226.

White RW, Powell R and Clarke GL (2002) The interpretation of reaction textures in Fe-rich metapelitic granulites of the Musgrave Block, central Australia, p. constraints from mineral equilibria calculations in the system K2O–FeO–MgO–Al2O3–SiO2–H2O–TiO2–Fe2O3. *Journal of Metamorphic Geology* **20**, 41–55.

White RW, Powell R, Holland TJB, Johnson TE and Green ECR (2014) New mineral activity–composition relations for thermodynamic calculations in metapelitic systems, p. *Journal of Metamorphic Geology* **32**, 261–86.

Williams ML and Grambling JA (1990) Manganese, ferric iron, and the equilibrium between garnet and biotite, p. *American Mineralogist* **75**, 886–908.

Yang HM, Kyser K and Ansdell K (1998) Geochemical and Nd isotopic compositions of the metasedimentary rocks in the La Ronge Domain Trans-Hudson Orogen Canada. Implications for evolution of the domain. *Precambrian Research* **92**, 37–64.

Yin A, Dubey CS, Wedd AAG, Kelty TK, Grove M, Gehrels GE and Burge WP (2010) Geologic correlation of the Himalayan orogen and Indian craton, p. Part I. Structural geology, U-Pb zircon geochronology, and tectonic evolution of the Shillong Plateau and its neighbouring regions in NE India, p. *GSA Bulletin* **122** (3/4), 336–59.

Zhang HT, Li JH, Liu SJ, Li WS, Santosh M and Wang HH (2012) Spinel + quartz bearing ultrahigh-temperature granulite from Xumayao, Inner Mongolia Suture Zone, North China Craton, p. petrology, phase equilibria and counterclockwise p-T path, p. *Geoscience Frontier* **3**, 603–11.

Zhao G, Cawood PA, Wilde SA and Lu LZ (2001) High-Pressure granulites (Retrograded Eclogites) from the Hengshan complex, North China craton: petrology and tectonic implications. *Journal of Petrology* **42**, 1141–70.

Zhao G, Sun M, Wilde SA and Li S (2004) A Paleo-Mesoproterozoic supercontinent: assembly, growth and breakup. *Earth-Science Reviews* **67**, 91–123.

Zhao L, Chen H, Zhang L, Zhang W, Yang J and Yan X (2018) The late Paleozoic magmatic evolution of the Aqishan-Yamansu belt, Eastern Tianshan: Constraints from geochronology, geochemistry and Sr–nd–Pb–hf isotopes of igneous rocks. *Journal of Asian Earth Sciences* **153**, 170–92.

Zhou MF, Kennedy AK, Sun M, Malpas J and Lesher CM (2002) Neoproterozoic arc-related mafic intrusions along the northern margin of South China: implications for the accretion of Rodinia. *The Journal of Geology* **110**, 611–8.